

Review

Multicomponent Metal Oxide- and Metal Hydroxide-Based Electrocatalysts for Alkaline Water Splitting

Gooun Lee ^{1,2,†} , Sang Eon Jun ^{1,3,†}, Yujin Kim ¹, In-Hyeok Park ² , Ho Won Jang ³ , Sun Hwa Park ^{1,*} and Ki Chang Kwon ^{1,*} 

¹ Smart Device Team, Interdisciplinary Materials Measurement Institute, Korea Research Institute of Standards and Science (KRISS), Daejeon 34133, Republic of Korea

² Graduate School of Analytical Science and Technology (GRAST), Chungnam National University, Daejeon 34134, Republic of Korea

³ Department of Materials Science and Engineering, Research Institute of Advanced Materials, Seoul National University, Seoul 08826, Republic of Korea

* Correspondence: psh@kriss.re.kr (S.H.P.); kichang.kwon@kriss.re.kr (K.C.K.)

† These authors contributed equally to this work.

Abstract: Developing cost-effective, highly catalytic active, and stable electrocatalysts in alkaline electrolytes is important for the development of highly efficient anion-exchange membrane water electrolysis (AEMWE). To this end, metal oxides/hydroxides have attracted wide research interest for efficient electrocatalysts in water splitting owing to their abundance and tunable electronic properties. It is very challenging to achieve an efficient overall catalytic performance based on single metal oxide/hydroxide-based electrocatalysts due to low charge mobilities and limited stability. This review is mainly focused on the advanced strategies to synthesize the multicomponent metal oxide/hydroxide-based materials that include nanostructure engineering, heterointerface engineering, single-atom catalysts, and chemical modification. The state of the art of metal oxide/hydroxide-based heterostructures with various architectures is extensively discussed. Finally, this review provides the fundamental challenges and perspectives regarding the potential future direction of multicomponent metal oxide/hydroxide-based electrocatalysts.

Keywords: alkaline water splitting; transition metal oxides; transition metal hydroxides; single-atom catalysts; electrocatalysts



Citation: Lee, G.; Jun, S.E.; Kim, Y.; Park, I.-H.; Jang, H.W.; Park, S.H.; Kwon, K.C. Multicomponent Metal Oxide- and Metal Hydroxide-Based Electrocatalysts for Alkaline Water Splitting. *Materials* **2023**, *16*, 3280.

<https://doi.org/10.3390/ma16083280>

Academic Editors: Laura Calvillo, Marcello Crucianelli and Andrea Lazzarini

Received: 22 February 2023

Revised: 10 April 2023

Accepted: 14 April 2023

Published: 21 April 2023



Copyright: © 2023 by the authors. Licensee MDPI, Basel, Switzerland. This article is an open access article distributed under the terms and conditions of the Creative Commons Attribution (CC BY) license (<https://creativecommons.org/licenses/by/4.0/>).

1. Introduction

Fossil fuels have been used as an energy source by humanity since the Industrial Revolution, but the depletion of energy sources and environmental damage caused by carbon dioxide emissions have made it essential to find new, clean, and sustainable energy sources. Hydrogen, which boasts a high mass-to-ignition heat and produces no carbon dioxide emissions, is considered one of the most promising sources of clean energy [1–6]. While hydrocarbon reforming remains the primary method of hydrogen production, accounting for 95% of industrial production, it emits carbon dioxide and is therefore known as “gray hydrogen”. Electrochemical water splitting, which uses renewable energy to produce hydrogen, is viewed as a more promising technology for “green hydrogen” production due to its zero-carbon footprint, simplicity, and high energy efficiency [7–13].

Water electrolyzers, which split water to produce hydrogen, come in various forms including proton exchange membrane (PEM) electrolyzers and alkaline anion exchange membrane electrolyzers. PEM devices require the use of noble metal catalysts, such as Pt and Ir, and are limited by their high cost and low durability in harsh environments [14–16]. On the other hand, earth-abundant non-precious metal catalysts, such as Ni, Co, and Fe, have great potential for low-cost and large-scale hydrogen production when used in alkaline anion exchange membrane electrolyzers [17–19]. In recent years, transition

metal oxides/hydroxides have emerged as efficient and stable electrocatalysts due to their high activity and stability [19–21]. Despite this, these catalysts face challenges such as low electrical conductivity, limited intrinsic activity, and a limited number of active sites. Multicomponent metal oxide/hydroxide electrocatalysts can overcome these limitations by combining multiple active sites and synergistic effects, resulting in improved catalytic performance. Researchers are exploring various methods to improve the catalytic properties of oxide/hydroxide-based multicomponent electrocatalysts, including interface engineering [22–24], alloying [25–27], doping [28–31], single-atom catalysts [32–34], and the development of phosphides [35,36], sulfides/selenides [37–39], and carbides/nitrides [40,41]. These methods aim to enhance the electronic structure, increase conductivity, optimize surface adsorbed species, and reduce energy barriers [42–46]. In particular, according to Sabatier's principle suggesting that a suitable adsorption Gibbs free energy should be optimized for high catalytic activity, it is necessary to investigate multicomponent catalysts possessing extraordinary surface adsorption that is hard to achieve in a single metal-based catalyst. For example, single-atom catalysts enable the formation of a multicomponent catalyst to use electronic interactions with the support matrix to create new geometric structures and reduce the energy barriers of catalytic reactions [47–50]. The resulting multicomponent oxide/hydroxide-based catalysts hold great promise for future applications due to their improved reaction rates, structural/performance stability, and overall effectiveness.

Herein, we provide an overview of the surface reaction mechanism and recent progress on multicomponent transition metal-based oxide/hydroxide electrocatalysts for alkaline water splitting. First, we will introduce some basic reaction mechanisms of hydrogen evolution reaction (HER) and oxygen evolution reaction (OER) in an alkaline media. Then, the synthetic methods and characterization of the state-of-the-art electrocatalysts will be presented. Finally, the challenges and perspectives will be discussed. This review would be useful in the field of material science and chemistry for the construction and fabrication of high-performance water-splitting catalysts.

2. Electrochemistry of Water Splitting in an Alkaline Environment

In conventional electrolysis, the efficiency of the process depends on the concentration of charge carriers, which are typically ions in the solution. An electrolysis system and possible reaction pathways for water splitting are shown in Figure 1. Under acidic conditions, the OER at the anode corresponds to the equation $2\text{H}_2\text{O} \rightarrow \text{O}_2 + 4\text{H}^+ + 4\text{e}^-$. The electrons flow through the external circuit, while the protons move across a membrane to reach the cathode compartment. Then the protons combine with the electrons to form hydrogen gas (H_2) through the HER: $4\text{H}^+ + 4\text{e}^- \rightarrow 2\text{H}_2$. At lower pH values, the kinetics of the water reduction is faster than in alkaline media due to the high concentration of protons (H^+). However, at higher pH values, the concentration of hydroxide ions (OH^-) is higher, which achieves the fast water oxidation reaction at the anode [51]. To drive the water-splitting reaction by overcoming the kinetic barriers of OER and HER, a minimum thermodynamic potential of 1.23 V is required. The role of electrocatalysts is crucial to reduce this overpotential as much as possible. Photo-electrochemical (PEC) water splitting is an attractive process as it utilizes sunlight as an energy source and emits no CO_2 [52]. Additionally, the use of a material with a bandgap above 1.23 eV enables water splitting to be achieved without requiring an external bias. However, the property of photocatalytic water splitting is often limited by the bandgap of the photocatalytic material, which determines its absorption spectrum and energy conversion efficiency [53]. In contrast, electrocatalytic water splitting can be achieved using a variety of electrocatalysts, including metal oxides, phosphides, and sulfides. While many materials can operate as electrocatalysts, the exact mechanism by which they work is not fully understood for all materials. Thus, gaining a deep understanding of the reaction mechanism and activity relationship of HER/OER is essential in the development of efficient catalysts for electrochemical water splitting [54].

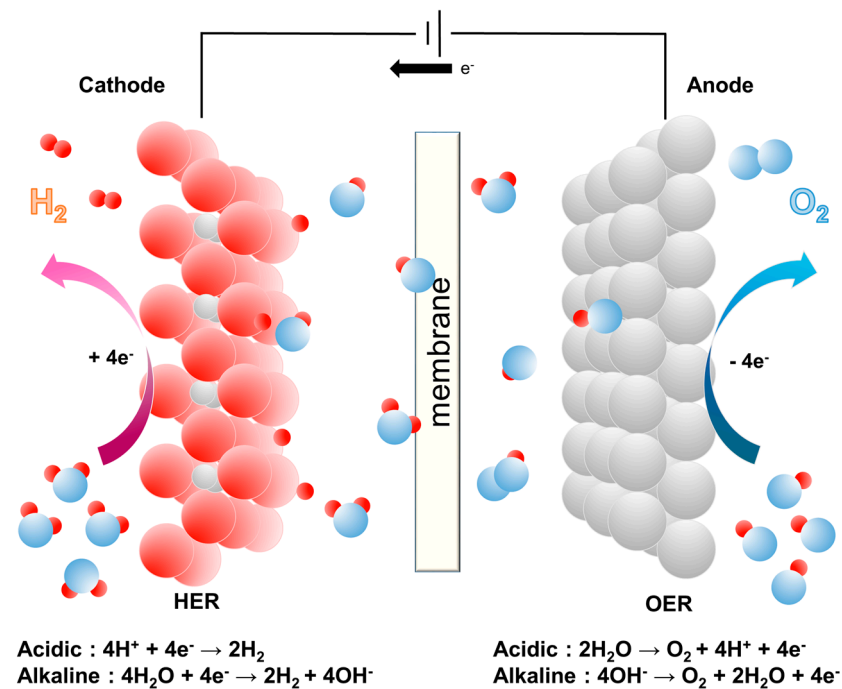


Figure 1. Schematic of the electrochemical water splitting and related reaction kinetics.

2.1. Mechanism of HER in Alkaline Media

In an alkaline media, the hydrogen evolution reaction (HER) is harder to achieve compared with acidic electrolytes due to the lower concentration of protons. The hydrogen intermediates (denoted as H^{*}) are mainly formed by the dissociation of water molecules in alkaline media, whereas in acidic media, they are derived from hydrogen protons (H⁺) [55,56]. This means that breaking the stronger covalent H–O–H bond in alkaline media requires more energy compared with the dative covalent bond of the hydronium ion (H₃O⁺) in acidic electrolytes. The first step of the HER process, denoted as the Volmer step, involves the adsorption of hydrogen intermediates on the surface of the electrocatalyst (Equation (1)).



There are two mechanisms for forming H₂ through either the Volmer–Heyrovsky or Volmer–Tafel step (Equations (2) and (3)).

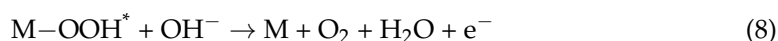
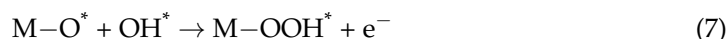


A good HER catalyst must have low Gibbs free energy for H^{*} adsorption and high exchange current density with many active sites [54,57,58].

2.2. Mechanism of OER in Alkaline Media

There is a more complicated mechanism and slower kinetics in the OER process compared with HER, which requires a four-electron transfer process [59–62]. In alkaline media, two different pathways of O₂ generation are possible: (i) the direct combining of adsorbed oxygen (O^{*}) at two M–O^{*} species (from M–OH^{*}) and (ii) the proton-coupled electron transfer (from M–OOH^{*}). The hydroxide anion (OH⁻) is adsorbed on the catalyst surfaces to form M–OH^{*}. M–OH^{*} is converted to M–O^{*} by coupling between H^{*} and OH⁻. Then, the combination of two M–O^{*} species directly produces an O₂ molecule and two free M active sites. There is another pathway to generate O₂ molecules by forming an M–OOH^{*} intermediate, which can be generated by combining M–O^{*} and OH⁻. In this pathway, an

additional proton-coupled electron transfer step requires the release of an O₂ molecule and the regeneration of the initial free active sites.



The second pathway generally occurs in the OER process. Achieving the low reaction Gibbs free energy between the catalyst surface and the OER intermediates (M-O* and M-OOH*) is important to improve the OER performance [56].

2.3. Strategies for Catalysts Design in Alkaline Media

Non-noble metal-based oxides/hydroxides are attractive catalysts for water electrolysis due to their abundance, low cost, adjustable structures, and stability [63–72]. However, their poor electrical conductivity and limited active sites hinder their electrocatalytic performance. To overcome these limitations, various strategies have been applied to oxide/hydroxide-based catalysts such as heterostructure engineering, doping, and anchoring single atoms. Through these approaches, the number of active sites where the reaction occurs increases, and the intrinsic conductivity of the catalysts can be improved [73–82]. The representative strategies to accomplish the advanced oxide/hydroxide-based catalysts are proposed in Figure 2.

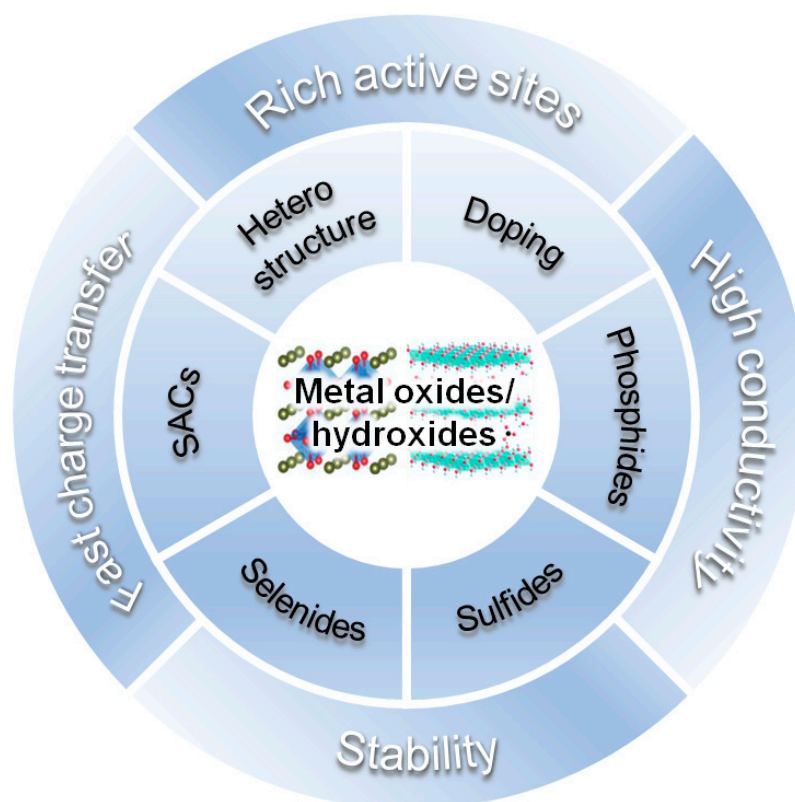


Figure 2. Proposed strategies to realize the improved alkaline water splitting by functionalities and advantages in multicomponent metal oxides and hydroxides.

2.3.1. Heterostructures

The heterostructure, defined as a composite structure consisting of two or more different solid-state materials with interfacial interaction, has attracted attention in the field of energy-related applications due to its unique interface that provides synergistic effects such as enhanced electrochemical activity and structural stability [83–86]. As an example, Zheng's group designed a well-defined heterointerface between Pt and LiCoO₂ [87]. The synergistic effects at the Pt/LiCoO₂ heterostructure interfaces enhance the Volmer step, which is a rate-determining step in the alkaline hydrogen evolution reaction (HER), by improving the capability of cleaving the HO–H bond. By optimizing the Pt–H bond affinity, fast hydrogen evolution can be achieved. In conclusion, heterostructured electrocatalysts are a promising strategy for improving intrinsic activity through the effective control of the geometric and electronic structure of the active site through interface engineering [88–91].

2.3.2. Doping

Elemental doping has been considered an effective way to enhance the catalytic performance of electrocatalysts. Heteroatom doping of foreign atomic structures can alter the chemical and physical properties of electrocatalysts, resulting in improved intrinsic catalytic activity [92–96]. The increased surface area and additional catalytic active sites are achieved through enhanced local charge and spin density from the difference in the electronegativity and atomic radii of the anion doping elements [97,98]. There is a wealth of previous research that shows the ability of water molecule adsorption and desorption on heteroatom-doped oxides/hydroxides [99–103]. The intrinsic OER performance can be improved by incorporating metal cations into NiFeM (M=Co, Mn, Cr, Al, etc.) catalysts. For example, Jiang's group found that V cations contribute to the high OER activity of NiFeOH by providing strong OOH* binding energy relative to O* species [98]. Van et al. successfully designed La-doped NiFe LDH using a hydrothermal method [104]. The strong electronic interactions between La and NiFe LDH elevate the Fe d-band level, increase the number of catalytic active sites and oxygen vacancies, and result in excellent OER activity. Therefore, heteroatom doping provides an ideal platform to modify various physicochemical properties such as phase transformation, vacancies, defects, and electronic band structures of oxide/hydroxide electrocatalysts [105–107].

2.3.3. SACs

Single-atom catalysts have recently attracted enormous research interest due to their high atomic utilization efficiency, unconventional catalytic activity, and high selectivity compared with their cluster and nanoparticle counterparts [108–116]. Depending on the support matrix interacting with the metal single atoms, the distinct local electronic structure and coordination environment of SACs can be achieved, enabling the strong activation of the reactants. Hence, SACs are versatile for surface-active electrochemical reactions such as HER, OER, oxygen reduction reaction (ORR), CO₂ reduction reaction (CO₂RR), nitrogen reduction reaction (NRR), etc. [117–125]. In these reactions, SACs provide large amounts of active sites where the reacting elements (H⁺, OH[−], O₂, CO₂, and N₂) participate. For example, Wang et al. introduced highly dispersed Ir single atoms with a concentration of about 3.6 wt% on an Ni₂P catalyst for OER, and they showed 28-fold higher OER efficiency compared with the most widely used IrO₂ catalyst [126]. It was revealed that Ir single atoms preferentially occupied Ni sites of Ni₂P, and the reorganized Ir–O–P/Ni–O–P bonding optimized the adsorption and desorption of the OER intermediate species. Consequently, the multicomponent electrocatalysts achieved by single-atomic active sites enable suppression of the intrinsic limits of metal oxide/hydroxide-derived materials by enlarging catalytically active sites with high metal utilization efficiency.

3. Multicomponent Oxide/Hydroxide-Based Electrocatalysts

Transition metal oxides/hydroxides, such as nickel oxide (NiO), cobalt oxide (CoO), and iron oxide (Fe₂O₃), have been widely studied for their potential use in the alkaline water-splitting reaction for hydrogen production [88,127–129]. These materials have several key properties that make them attractive for water splitting. Transition metal oxides/hydroxides showed high chemical stability in alkaline environments and excellent catalytic activity toward both HER and OER [130–133]. It is also considered a relatively low-cost catalytic material compared with novel metal ones. However, it has several limitations for following reasons: (i) the poor long-term stability due to degradation and loss of active sites in the redox process in OER, (ii) the limited stability under high overpotential conditions, and (iii) the low efficiency and high energy consumption because of the high overpotential required for the OER. Although the transition metal oxides/hydroxides show promising potential for utilization in alkaline water splitting, further research is needed to address the above limitations and improve their stability and efficiency for practical applications [134,135]. In this section, we will provide several distinct strategies to improve not only the catalytic performance in alkaline water splitting but also the long-term stability.

3.1. Transition Metal Oxides/Hydroxides

The advantages of heterostructure and single-atomic active sites can be simultaneously applied to the metal oxide catalysts. The heterointerface not only acts as the catalytic site where water dissociation occurs but also provides favorable anchoring sites to single-atomic metals. Zhou et al. fabricated Pt single-atom (Pt_{SA})-NiO/Ni nanosheets on Ag nanowires through a simple hydrothermal method, in which three-dimensional (3D) morphology boosted the electric conductivity and abundant active sites' accessible channels for charge transfer [136]. The proposed HER process and water dissociation on Pt_{SA}-NiO/Ni are illuminated in Figure 3a. The metallic Ni and O vacancies-modified NiO sites near Pt_{SA}-NiO/Ni at the interfaces of NiO/Ni heterostructure preferred adsorption affinity toward OH[•] and H[•], respectively, which can be calculated by the energy barrier in the Volmer step. The high-angle annular dark-field scanning transmission electron microscopy (HAADF-STEM) image (Figure 3b) displays the immobilization of atomically dispersed Pt atoms (bright spots) along with the interfaces of the NiO/Ni heterostructure. The most of single Pt atoms are strongly anchored at the interfaces of the NiO/Ni heterostructure. Although the emission of hydrogen bubbles during the Pt_{SA} electrodeposition process can degrade the fabricated heterostructures, there are no obvious morphology changes in Pt_{SA}-NiO/Ni nanosheets on Ag NWs compared with the original NiO/Ni surfaces, indicating the enhanced catalytic activity as well as high stability via the more active sites' high structural stability. In Figure 3c, the X-ray absorption near edge structure (XANES) spectra of Pt L3-edge with each support are provided to reveal 5d occupancy of Pt since the intensity of the white-line peak indicates the transfer of the Pt 2p_{3/2} core electron to 5d states. From the XANES spectra, it was confirmed that the charge loss of Pt_{SA}-NiO/Ni is higher than that of Pt_{SA}-Ni and lower than that of Pt_{SA}-NiO, as displayed in Figure 3c. From the calculated Pt oxidation states derived from the ΔXANES spectra, the average valence states of Pt were +0.29, +0.73, and +1.23 for Pt_{SA}-Ni, Pt_{SA}-NiO/Ni, and Pt_{SA}-NiO, respectively. Charge delocalizing from Pt to the bonded O atom and charge localizing from the adjacent Ni atoms to Pt are displayed due to the different electronegativity of atoms (3.44 for the O atom, 1.91 for Ni, and 2.28 for Pt). Consequently, an enhanced electric field with a half-moon shaped area around the Pt site (Figure 3d) suggests that the NiO/Ni heterostructure coupled with a Pt single atom could possess more free electrons to promote the adsorbed H conversion for high H₂ evolution reaction.

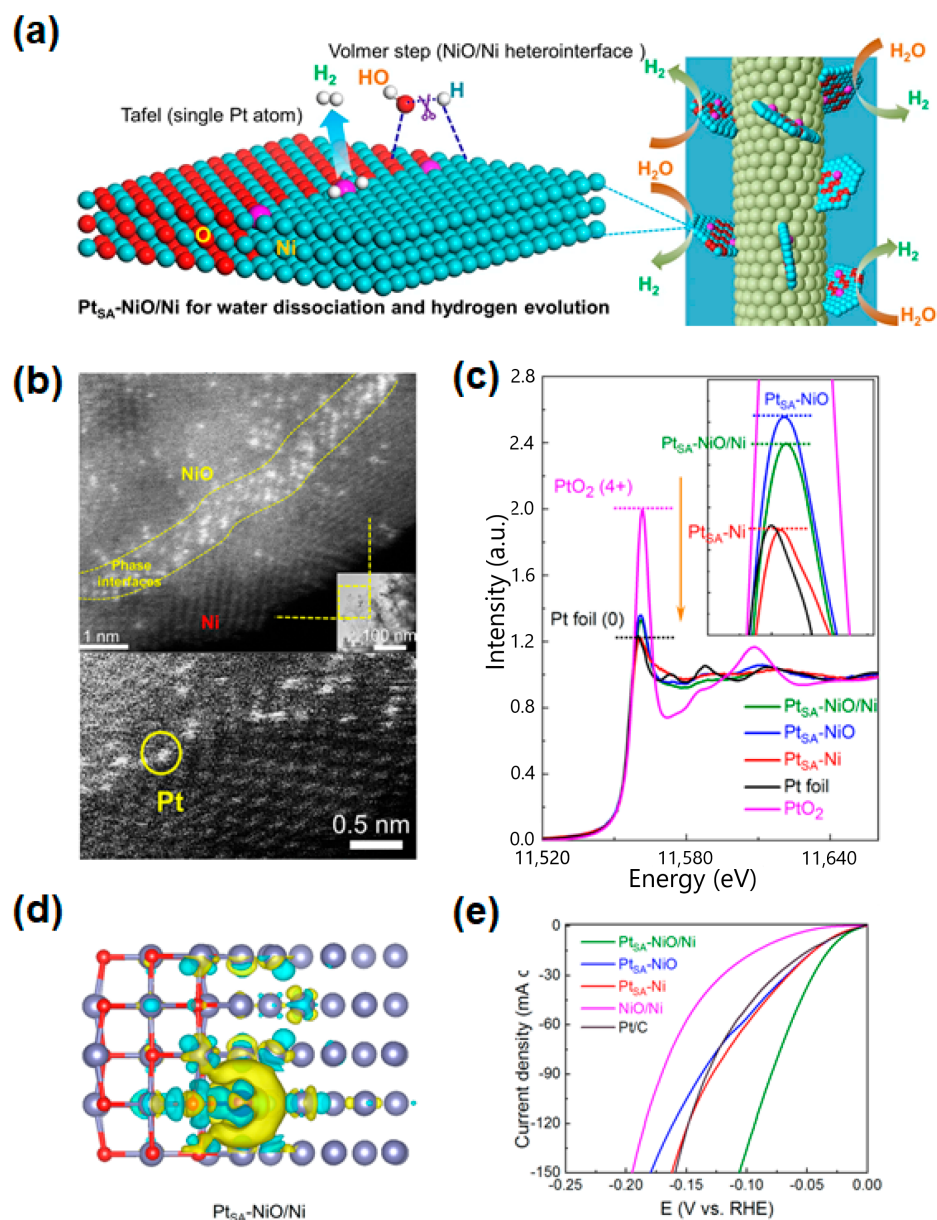


Figure 3. (a) The mechanism of the $\text{Pt}_{\text{SA}}\text{-NiO/Ni}$ network as an efficient catalyst toward large-scale water electrolysis in alkaline media. (b) HAADF-STEM image of $\text{Pt}_{\text{SA}}\text{-NiO/Ni}$. (c) XANES spectra and calculated Pt oxidation states derived from ΔXANES spectra of $\text{Pt}_{\text{SA}}\text{-NiO/Ni}$, $\text{Pt}_{\text{SA}}\text{-NiO}$, and $\text{Pt}_{\text{SA}}\text{-Ni}$, with Pt foil given as a reference. (d) Computational models and localized electric field distribution of a $\text{Pt}_{\text{SA}}\text{-NiO/Ni}$. (e) LSV curves of $\text{Pt}_{\text{SA}}\text{-NiO/Ni}$, $\text{Pt}_{\text{SA}}\text{-NiO}$, $\text{Pt}_{\text{SA}}\text{-Ni}$, NiO/Ni , and Pt/C for HER. Reprinted (adapted) from reference [136], copyright (2021) Springer Nature.

The $\text{Pt}_{\text{SA}}\text{-NiO/Ni}$ shows the best HER intrinsic activity compared with other reference samples (Figure 3e), a significantly lower overpotential of 26 mV at 10 mA/cm², which is superior to even the commercial Pt/C catalyst (52 mV at 10 mA/cm²). As the advantage of single-atom catalysts, they conducted the mass activity comparison of fabricated samples. The normalized mass activity to the loaded Pt mass of the $\text{Pt}_{\text{SA}}\text{-NiO/Ni}$ sample was 20.6 A/mg at an overpotential of 100 mV, which is 2.4, 2.3, and 41.2 times greater than that of $\text{Pt}_{\text{SA}}\text{-NiO}$ (8.5 A/mg), $\text{Pt}_{\text{SA}}\text{-Ni}$ (9.0 A/mg), and the commercial Pt/C catalyst (0.5 A/mg), respectively. Furthermore, the $\text{Pt}_{\text{SA}}\text{-NiO/Ni}$ catalyst exhibited a lower Tafel slope value, 27.07 mV/dec, than the $\text{Pt}_{\text{SA}}\text{-NiO}$ (37.54 mV/dec), $\text{Pt}_{\text{SA}}\text{-Ni}$ (37.32 mV/dec), NiO/Ni (58.67 mV/dec), and Pt/C catalysts (41.69 mV/dec). In the stability test, the $\text{Pt}_{\text{SA}}\text{-NiO/Ni}$ catalysts showed high durability with negligible degradation in cyclic tests over 5000 cycles and in chronopotentiom-

etry for 30 h. These highly durable and efficient Pt_{5A}-based electrocatalysts could be achieved by anchoring on highly stable NiO/Ni heterointerfaces. From these series of theoretical and experimental results, the Pt SACs coupled with NiO/Ni heterointerfaces could boost the HER catalytic activity in an alkaline environment, leading to a significant reduction in cost. This work provides a facile way to design not only noble metal-base SACs but also the heterostructures for efficient alkaline HER.

The doping of the proper amount of noble metal can improve the catalytic activity of metal oxide catalysts. In particular, the Ru element possesses the capability to effectively dissociate H₂O into H⁺ and OH⁻, thereby allowing for optimal hydrogen production in an alkaline condition through doping. Zhang and colleagues developed a three-dimensional (3D) needle-like array of Ru-doped Ni/Co oxides (Ru-NiO/Co₃O₄) based on a carbon cloth (CC) substrate via a three-step process [137]. First, Ni_{0.5}Co_{0.5}(OH)₂ (NCO) nanoneedle arrays were synthesized on the surface of CC through the hydrothermal method. By controlling the Ru concentration, various Ni_{0.5}Co_{0.5}(OH)₂ structures were obtained for xRu-NCO by Ru³⁺ immersion. Finally, they obtained Ru-NiO/Co₃O₄ nanoneedle structures after an oxidation process at 400 °C in an N₂ environment. The morphology of the as-prepared electrocatalyst was characterized by a scanning electron microscope (SEM), as shown in Figure 4a. The lamellar morphology of Co₃O₄ was almost broken and cracked because the annealing treatment at high temperatures resulted in the collapse of the hydroxide structure due to the removal of water molecules, but the Ni-added NCO could maintain the needle-like array structure after oxidation. With the insertion of a high concentration of Ni content, the needle structure of NiO/CC would be denser and shorter than NCO. The staggered distribution of Co₃O₄ and NiO implies the creation of a large number of interfaces and high-energy regions, which can modulate the overall electronic energy state and expose a large number of active sites. The Ru 2% doped-NCO, which has the largest geometrical area with dense and uniform needle-like arrays, facilitates a sufficient contact area between the catalyst and the electrolyte, resulting in high-performance water splitting. As displayed in Figure 4a, HAADF-STEM images clearly show the presence of RuO₂ particles with about 5 nm diameter inside needle-shaped NCOs. From the XPS O 1s core level spectra, Ru 2% doped-NCO (529.8 eV) still has the lowest anion binding energy compared with the other samples (Figure 4b) by constructing oxygen bonding between Ru atoms and oxygen vacancies. Based on these measurements, Ru doping and the NCO heterostructure system would exhibit higher catalytic activity by controlling the overall electronic energy state of the catalyst, influencing faster charge transport kinetics. From the Raman spectra, they confirmed that the heterogeneous structure of NCO and the Ru doping induces more defects. Among the various xRu-NCO samples, the 2% Ru-NCO electrocatalysts showed the best catalytic OER performance with the lowest overpotential of 233 and 269 mV at a current density of 50 and 100 mA/cm² due to the densest and uniform morphology and proper distribution of RuO₂ with 5 nm nanoparticles (Figure 4c). For the Tafel slope, the smallest Tafel slope value of 59 mV/dec could be obtained by fast OER kinetics originating from the fastest energy conversion and small activation energy to conduct OER. Furthermore, the 2% Ru-NCO showed excellent durability in both the cyclic test and chronopotentiometry measurement. There is a negligible potential shift in cyclic LSV tests after 1000 cycles, and only a 1.8% decayed overpotential value could be observed after 25 h of continuous operation. From the XRD and TEM analysis, the diffraction peak and crystal structure have not been changed in 2% Ru-NCO electrocatalysts after OER operation. They also investigated the HER and overall water-splitting performance of a 2% Ru-NCO electrocatalyst. It achieved a low overpotential of 51 and 138 mV at current densities of 10 and 100 mA/cm², which is superior to that of Pt/C (52 and 156 mV at 10 and 100 mA/cm²). In the stability test, the 2% Ru-NCO showed good durability in the cyclic test over 10,000 cycles with negligible shifts and 3.4% decayed current density after 25 h of continuous operation. By utilizing 2% Ru-NCO samples as both cathode and anode in alkaline media (1 M KOH), the required potential to drive the overall water splitting up to 50 and 100 mA/cm² was 1.57 V and 1.64 V with highly stable operation

properties over 25 h, as shown in Figure 4d. This improved catalytic activity and stability of 2% Ru-NCO can be attributed to (i) a large number of active sites by uniformly dispersed nanostructures, (ii) low activation energy to generate NiO/Co₃O₄ heterointerfaces and electronic energy state modulation by Ru doping, and (iii) tight bonding between NiO/Co₃O₄ heterostructures and Ru dopants. This work highlights the effect of controlling the heterogeneous structures and noble Ru metal doping on water-splitting performance using metal oxide-based electrocatalysts.

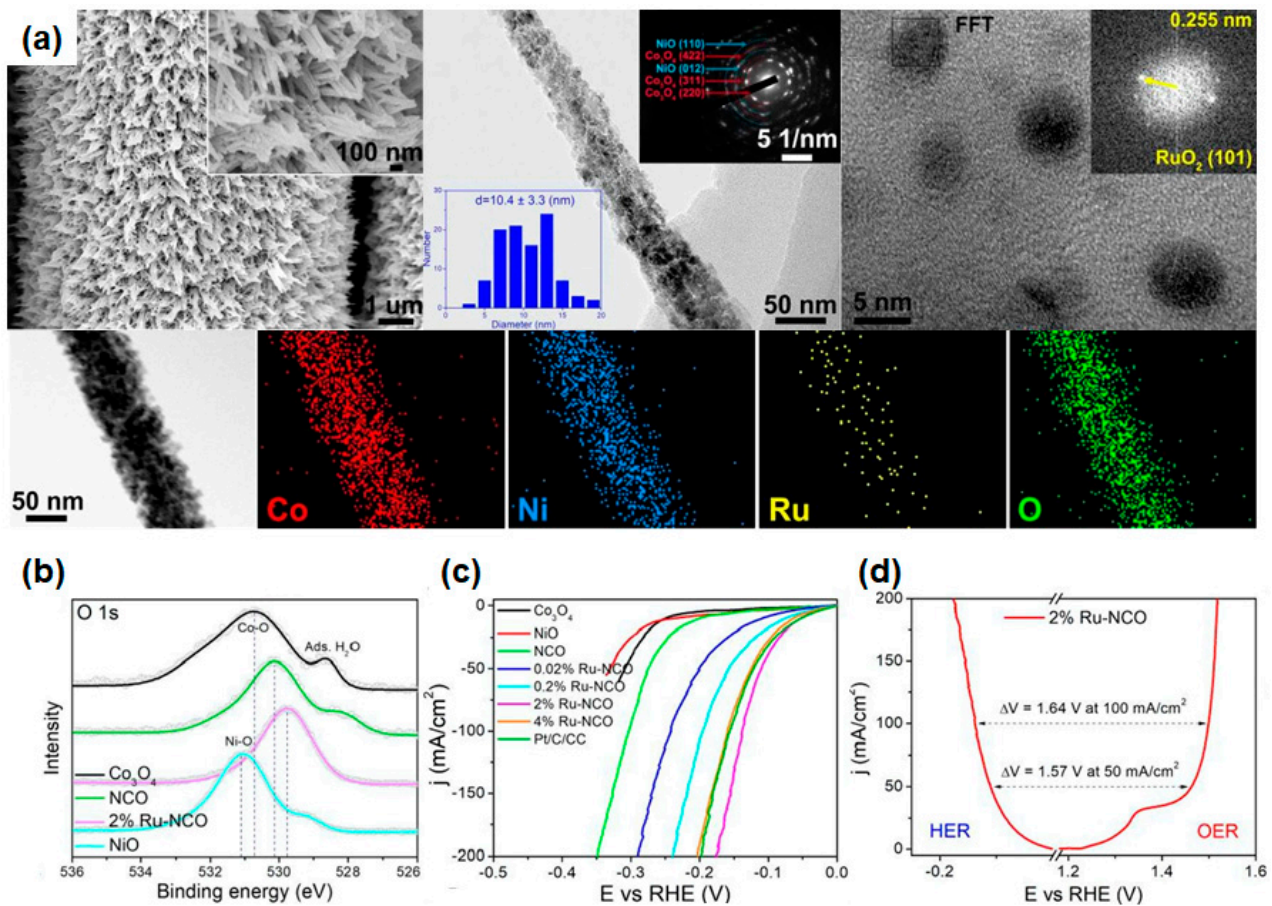


Figure 4. (a) (left) SEM and (middle) TEM images of 2% Ru-NCO with high magnification images. The corresponding SAED pattern and histogram of particle size distribution are also presented. (right) HR-TEM image of RuO₂ particles with the corresponding SAED pattern of the selected area. Elemental mapping images for Co, Ni, Ru, and O (below). (b) XPS patterns for Co₃O₄, NCO, 2% Ru-NCO, and NiO in O 1s core level spectra. (c) HER LSV curves of Co₃O₄, NiO, NCO, 0.02% Ru-NCO, 0.2% Ru-NCO, 2% Ru-NCO, 4% Ru-NCO, and RuO₂/CC in 1.0 M KOH. (d) LSV curves of 2% Ru-NCO for HER and OER in a three-electrode configuration. Reprinted (adapted) from reference [137], copyright (2022) Elsevier B.V.

Liu et al. approached two distinct strategies for synthesizing the Ce(OH)₃-interfaced NiFe-LDH (Ce@NiFe-LDH) and the homogeneously Ce-doped NiFe-LDH (CeNiFe-LDH) catalysts on Ni foam substrate using a hydrothermal process as shown in Figures 4b and 5a [138]. From the SEM measurements, the vertically and densely grown Ce@NiFe-LDH and CeNiFe-LDH could be observed with a similar nanosheet morphology of uniform thickness (~10 nm). The numerous nanoparticles could be observed in Ce(OH)₃ decorated on the surface of NiFe-LDH, whereas a smooth surface with stacked nanosheet structures was observed in the case of CeNiFe-LDH from the HR-SEM images. The average size of the decorated nanoparticles was 7 nm without aggregation, and the (101) and (012) lattice planes could be indexed to Ce(OH)₃ and NiFe-LDH in SAED patterns, respectively, as shown in Figure 5b.

HAADF-STEM images showed the corresponding element mapping of both samples. The Ce atoms are found intensively in particle form in Ce@NiFe-LDH, but in the CeNiFe-LDH nanosheets, they are spread over entirely. Furthermore, an additional peak revealed in Ce@NiFe-LDH originated from the (101) facet of Ce(OH)₃, indicating the coexistence of Ce(OH)₃ and NiFe-LDH nanosheets as shown in Figure 5c from the XRD spectra. Due to the amorphous structure, both CeNiFe-LDH and NiFe-LDH exhibit no other crystalline phases, demonstrating that metal atoms are homogeneously distributed in the crystal structure of α -Ni(OH)₂. They explained how the introduced Ce atoms could have enhanced the OER catalytic activity in terms of electronic interplay using orbital occupation between the metal and oxygen atoms, as shown in Figure 5d. The introduced Ce atoms in their structures could act as electron-accepting sites. As a result, the electron-deficient d-orbitals of Ce³⁺ strengthen the electron-accepting ability from O²⁻ to Ce³⁺, resulting in changes in the electronic structure of metal ions and influence of the OER catalytic activity in these trimetallic (oxy)hydroxides.

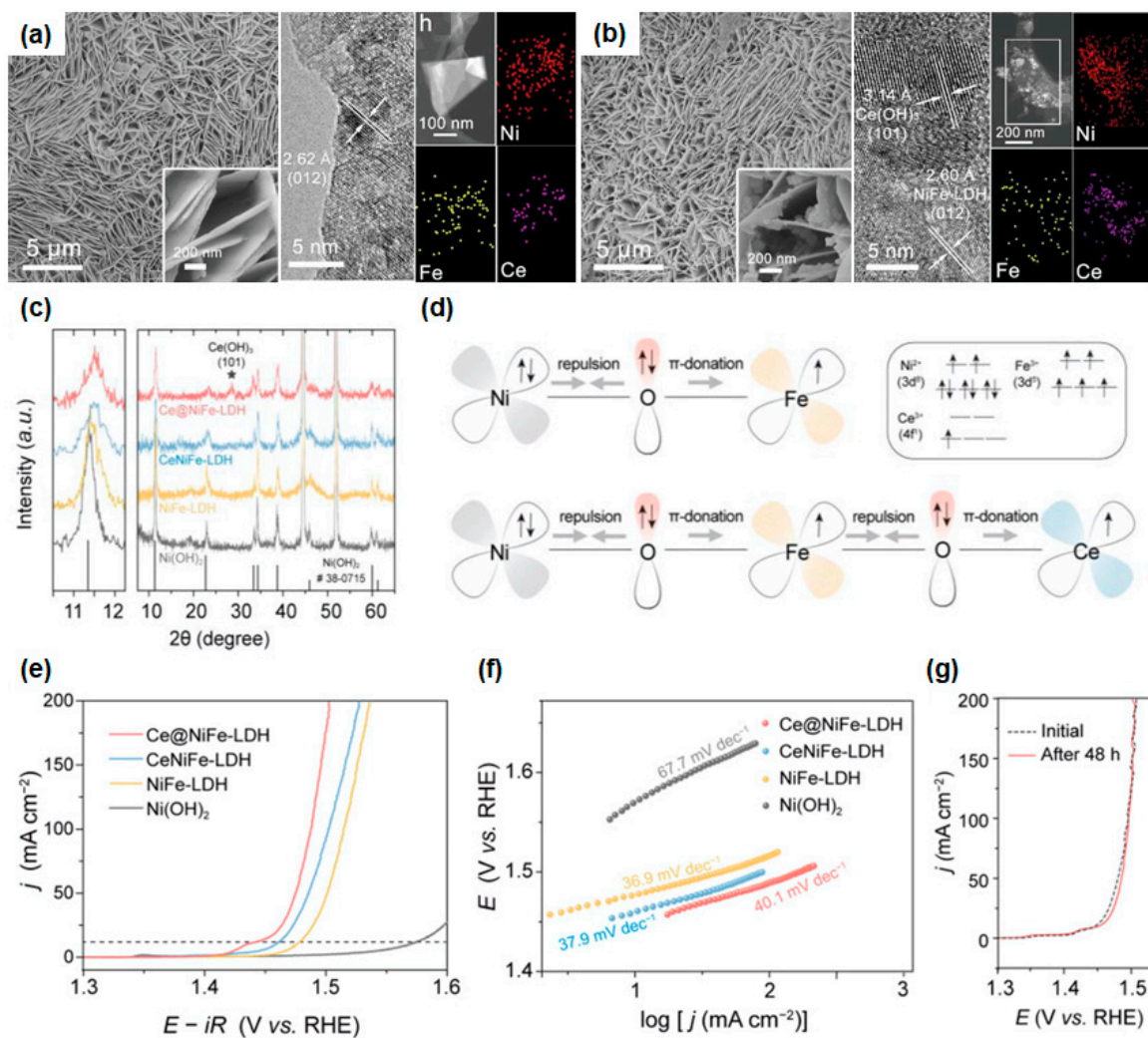


Figure 5. SEM, high-resolution TEM, HAADF-STEM images, and the corresponding EDX elemental mappings of (a) CeNiFe-LDH and (b) Ce@NiFe-LDH nanosheets. (c) XRD patterns of as-prepared Ce@NiFe-LDH and CeNiFe-LDH. The data for Ni(OH)₂, NiFe-LDH, and Ce(OH)₃ are shown for comparison. (d) Schematics of the electronic interplay among Ni, Fe, Ce, and O in NiFe-LDH, CeNiFe-LDH, and Ce@NiFe-LDH. (e) LSV curves. (f) The corresponding Tafel plots of Ce@NiFe-LDH, CeNiFe-LDH, NiFe-LDH, and Ni(OH)₂ for OER. Measured O₂ yields at 0.3 V. (g) LSV curves of Ce@NiFe-LDH before and after 48 h electrolysis. Reprinted (adapted) from reference [138], copyright (2021) Wiley-VCH GmbH.

Ce@NiFe-LDH achieved the best OER performance with low overpotentials of 205 and 257 mV at 10 and 100 mA/cm², respectively, and CeNiFe-LDH also showed good OER performances with an overpotential of 229 mV at 10 mA/cm², as shown in Figure 5e. The Tafel slopes of Ce@NiFe-LDH and CeFeNi-LDH are 40.1 and 37.9 mV/dec, which can compare with that of NiFe-LDH nanosheets, originating from the increased carrier concentration and conductivity due to the presence of Fe and Ce atoms (Figure 5f). From the cyclic LSV measurement, excellent stability with negligible degradation could be observed after 48 h of operation at 1.53 V, as shown in Figure 5g. They carried out the DFT calculations to acquire the Gibbs free energies along the OER pathway at U = 1.23 V. In the atomic model, the Ni sites of NiFe-LDH, CeNiFe-LDH, and Ce@NiFe-LDH (110) surfaces were selected as the active regions on which the OH^{*}, O^{*}, and OOH^{*} were preferentially adsorbed. The RDS of CeNiFe-LDH was the step from OOH^{*} to O² (g), whereas those of NiFe-LDH and Ce@NiFe-LDH were the step from OH^{*} to O^{*} due to the dissimilar surface charge configuration. The energy barrier of Ce@NiFe-LDH (0.56 eV) was lower than those of NiFe-LDH (0.92 eV) and CeNiFe-LDH (0.61 eV), implying that the thermodynamically favorable catalytic reaction occurs most actively in Ce@NiFe-LDH. This work demonstrated the facile route to increase the catalyst activity of NiFe LDHs by transition metal doping. By the deep understanding of OER mechanisms, the lower energy barrier in Ce@NiFe-LDH can provide not only the catalytic active sites but also stable OER performance.

Ru enables the effective dissociation of H₂O into H⁺ and OH⁻, leading to the enhanced catalytic activity of LDHs in alkaline conditions. In recent years, single-atomic Ru has received much attention since it exhibits higher activity and atomic utilization efficiency than Ru particles due to the unique oxidation state and coordinations. In this context, incorporating single atoms of Ru into a binary CoV-layered double hydroxide (LDH) porous nanosheet array allows the design of improved electrocatalysts. Zeng et al. reported the electronic structure engineering of the binary CoV LDH porous nanosheet array with a single atom of Ru [139]. The CoV and CoVRu LDH nanosheet array was fabricated using a one-step hydrothermal method on Ni foam. A 3D interconnected hexagonal nanosheet array (about 700 nm) was synthesized uniformly on Ni foam, as seen in SEM and TEM images, as displayed in Figure 6a. The porous structure of the CoVRu LDH can be demonstrated from the evolution of NH₃ and CO₂ gases during the hydrothermal process, and the single atoms of Ru in their structure can be attributed to improved catalytic activity. The interplanar spacing of 0.25 nm, indexed to the (012) plane of CoV LDH, shows that the introduction of Ru does not affect the lattice spacing due to the similar ionic radius of Ru³⁺ (68 pm), V³⁺ (64 pm), and Co²⁺ (65 pm), as shown in Figure 6a. The localized electronic structures and atomic coordination of Ru atoms are revealed by XANES and X-ray absorption fine structure (EXAFS). The Ru adsorption edge (Ru K-edge) of CoVRu LDH was observed between Ru metal and RuO₂, indicating a chemical valence state of Ru_{x+} (0 < x < 4), as shown in Figure 6b. The Fourier transform (FT) EXAFS curve of the Ru K-edge spectra of RuCoV LDH shows that the local atomic coordination of Ru is mainly from Ru–O bonds, not Ru–Ru or Ru–O–Ru bonds. These findings prove that isolated Ru single atoms form strong electronic bonds with CoV LDHs through coordination with O atoms, as illustrated in Figure 6c. The single Ru atom-anchored CoV LDH exhibited excellent HER catalytic activity and high OER catalytic performance with low overpotentials of 28 mV at 10 mA/cm² for HER and 263 mV at 25 mA/cm² for OER, as shown in Figure 6d. Furthermore, the CoVRu LDH had a significantly low Tafel slope of 25.4 mV/dec for HER, much lower than CoV LDH (109.3 mV/dec) and Ni foam (131.1 mV/dec), as depicted in Figure 6e. For OER, the Tafel slope was 74.5 mV/dec, indicating faster kinetics than other samples. The durability of the synthesized CoVRu LDH was evaluated with 2000 cycles for both HER and OER, showing excellent stability and maintaining the initial performance without attenuation. The overall water-splitting performance was evaluated using a CoVRu LDH || CoVRu LDH coupled electrode, requiring only 1.52 V cell voltage to achieve a current density of 10 mA/cm², compared with Pt/C || RuO₂ (1.56 V) and CoV LDH || CoV LDH (1.79 V). The favorable modulation of the electronic structure and local atomic coordination for the Ru

single-atom-anchored CoV LDH electrocatalysts can be possible through DFT calculations and XPS/XAS analysis. This work suggests that improved electrocatalytic activity of Co-based LDH can be achieved by single-atom catalysts for electrochemical water splitting.

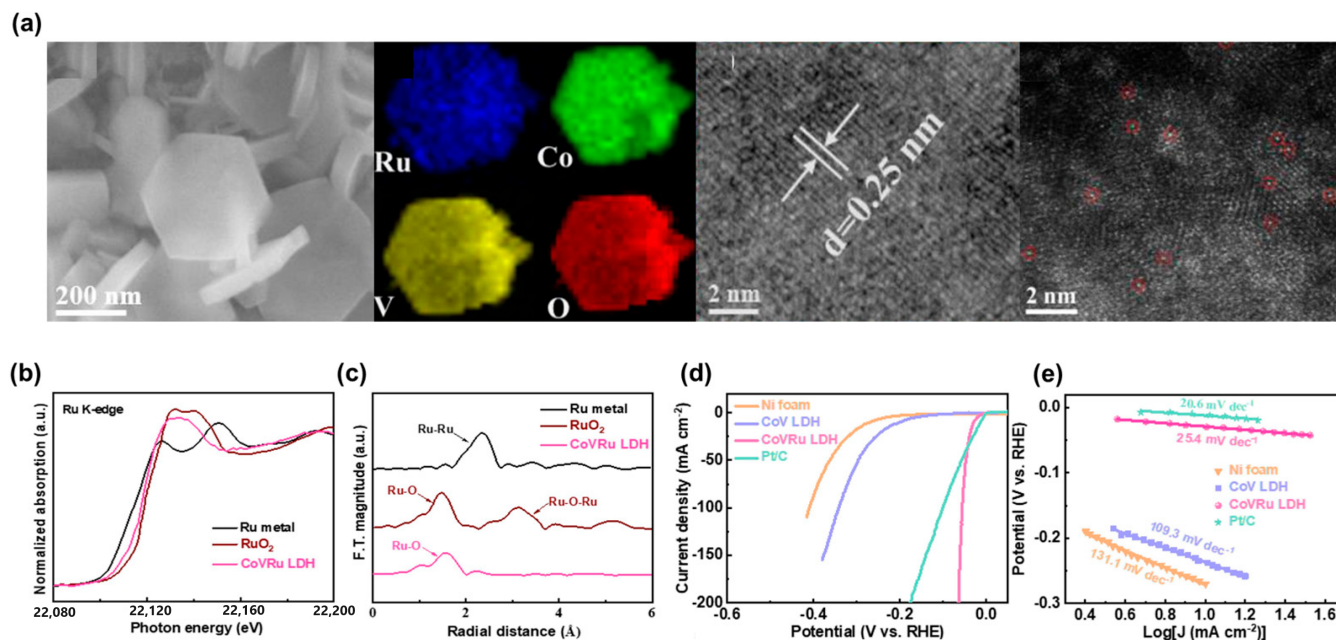


Figure 6. (a) SEM image (left) of hexagonal nanoplatelets of synthesized CoVRu LDH. STEM elemental mapping images with Ru, Co, V, and O. HR-TEM and HAADF-STEM images with d-spacing of 0.25 nm and atomically dispersed Ru sites, which are highlighted by red circles in CoVRu LDH. (b) Normalized XANES spectra and (c) Fourier-transformed EXAFS spectra of Ru K-edge for Ru metal, RuO₂, and CoVRu LDH. (d) HER polarization curves and (e) calculated Tafel slope graph. Reprinted (adapted) from reference [139], copyright (2023) Elsevier B.V.

3.2. Transition Metal Oxide-Based Derivatives

Transition metal oxide-based derivatives, such as transition metal phosphides, sulfides/selenides, and carbides/nitrides, are widely studied as catalysts for alkaline water splitting [137,140–143]. They have advantages and disadvantages compared with traditional catalysts such as noble metals. Some of the advantages of these derivatives include lower cost, higher stability, corrosion resistance, and environmental friendliness. They are useful in a wide range of applications not only in electrocatalysis but also in energy storage and electronic devices. The durability of metal oxide/hydroxide catalysts in alkaline water splitting is an important factor in determining their potential for practical applications. When the metal oxide/hydroxide catalysts are exposed to harsh conditions, including high pH, high temperature, and corrosive electrolytes, they can be degraded over time. To enhance the durability of metal oxide/hydroxide catalysts, several strategies can be employed, such as protective coatings, the development of a more stable composition, the optimization of the reaction conditions, and chemical modifications. Furthermore, some disadvantages include lower efficiency, limited selectivity in catalytic reactions, and the need for a proper synthesis method to achieve the desired properties. Despite these disadvantages, metal oxide/hydroxide-based catalysts are still considered as one of the promising catalysts to utilized water-splitting electrocatalysts. These catalysts are still an active area of research, and further developments may lead to improved performance and greater commercial viability [144,145]. In this section, we will introduce some strategies to enhance the catalytic activity and durability of metal oxide/hydroxide-based catalysts via chemical modification.

3.2.1. Transition Metal Phosphides

Transition metal phosphides (TMPs) have gained significant attention in the fields of catalysis and energy conversion due to their high catalytic activity, good thermal stability, cost-effectiveness, unique electronic properties such as high carrier mobility and high optical absorption, and high surface area [146,147]. However, several disadvantages must be addressed for the efficient use of TMPs as electrocatalysts, including poor stability in acidic conditions, limited selectivity for oxygen evolution reaction (OER), a lack of understanding of reaction mechanisms, and the cost ineffectiveness of the synthesis process [148–150]. In the following section, an example of designing a TMP-based electrocatalyst for overall water splitting will be provided.

Yu et al. demonstrated the efficient hybrid Fe-CoP/Ni(OH)₂ electrocatalysts, which showed high catalytic activity in HER, OER, and overall water-splitting ability in the alkaline environment [151]. The hybrid Fe-CoP/Ni(OH)₂ array electrode was fabricated through a coupled reaction, as shown in Figure 7a. Fe-CoP/Ni(OH)₂ NW arrays with a few micrometer lengths have grown on the NF substrate with a corn-shaped cluster through hydrothermal synthesis. The porous Fe-CoP NW array was synthesized by the pyrolytic phosphidation process; last, the ultrathin Ni(OH)₂ nanosheet could be electrodeposited on the outer surface of the Fe-CoP NWs. Their rational design facilitated easy access to reactants in the solution and helped the electron transfer in their heterostructures. From the TEM images in Figure 7b, the ultrathin Ni(OH)₂ nanosheets grown on the surface and apex of Fe-CoP NWs formed a heterostructure of individual clusters. The uniform distribution of Co, Fe, and P atoms was observed in HADDF-STEM and EDS mapping images, as shown in Figure 7a. The lattice fringe with 0.29 nm corresponding to the Fe-CoP (011) facet was observed before and after Ni(OH)₂ electrodeposition, indicating that heterostructure formation between Fe-CoP NWs and Ni(OH)₂ was performed without structural degradation. The similar d-spacing of Fe-CoP and Ni(OH)₂ facilitates forming their intimate contacts, which are large interfacial regions. The theoretically calculated Fe-CoP/Ni(OH)₂ interface suggests significant charge accumulation in the interfacial region due to strong charge redistribution. The electron density increases around the interfacial Co region and depletes in the interfacial Ni region, and these electronic interactions will help to strengthen the interaction of the reactants with the catalyst surface. LDOS (black dotted line) filled with the Fe-CoP component means that it provides most of the catalytic sites. In particular, the synergistic LDOS of the Fe-CoP/Ni(OH)₂ hybrid was significantly increased after incorporation with Ni(OH)₂.

This efficient heterostructure clearly showed a substantially improved catalytic performance in HER and OER characterization. The overpotential of Fe-CoP/Ni(OH)₂ was 91 mV at 10 mA/cm², and the Tafel slope was 48 mV/dec in HER using 1 M KOH electrolytes, which is comparable to commercial Pt/C catalysts, as shown in Figures 6d and 7c. Furthermore, the Fe-CoP/Ni(OH)₂ hybrid electrode exhibited good durability cyclic tests over 1000 cycles and 12 h of chronoamperometry with negligible current deterioration and morphology changes. They conducted theoretical calculations to confirm the superiority of the designed hybrid catalyst in HER. From the DFT calculations, the water adsorption energy of the Fe-CoP/Ni(OH)₂ hybrid surface (ΔG_{ad}) was calculated to be -0.65 eV, which was a more negative value than that of the Fe-CoP surface (-0.5 eV), suggesting that the water molecule was more energetically favorable to adsorb on the hybrid surface, as shown in Figure 7e. Furthermore, in Figure 7f, the Fe-CoP/Ni(OH)₂ hybrid catalyst exhibited a significantly decreased adsorption of reactant (H₂O) on the catalyst surface ($\Delta G(H_2O)$) value compared with that of Fe-CoP catalyst, suggesting an effective role of Ni(OH)₂ in promoting the dissociation of H₂O.

For the OER, the Fe-CoP/Ni(OH)₂ also showed excellent electrochemical properties with an overpotential of 206 mV at 10 mA/cm² and a Tafel slope of 32 mV/dec, as shown in Figures 6i and 7h, which is superior to the commercial OER catalyst RuO₂. There are three aspects that are expected to improve the OER catalytic activity of the Fe-CoP/Ni(OH)₂: (i) additional catalytic active sites from Ni(OH)₂ nanosheets, (ii) fast charge transport due

to electronic interaction between two different constituents, and (iii) lower energy barrier to adsorb the H_2O or intermediates from interfacial edge regions. To clarify the effect of the heterostructure in OER activity, they conducted the DFT calculations with four intermediate steps. From the Gibbs free energy diagram of the Fe-CoP/Ni(OH)₂ hybrid surface, as shown in Figure 7j, the lower $\Delta G(\text{HOO}^* = 1.77 \text{ eV})$ can be observed compared with that of the Fe-CoP $\Delta G(\text{HOO}^* = 2.08 \text{ eV})$, indicating the energetically favorable adsorption of the HOO^* intermediate on the hybrid surface can occur. It greatly helps to accelerate the OER kinetics, resulting in the promotion of the whole OER process. During the stability test, the hybrid electrode could maintain 92% of its initial current density at 1.5 V after 12 h. By assembling the hybrid catalysts as both cathode and anode, a two-electrode alkaline electrolyzer can be demonstrated. It exhibited the low cell voltages of 1.52 V and 1.59 V to reach the current densities of 10 and 50 mA/cm^2 , respectively, compared with the Pt/C || RuO₂ system (1.55 and 1.66 V for 10 and 50 mA/cm^2). These proposed hybrid catalysts shed light on the possibility to improve catalysts based on earth-abundant and non-noble transition metals for commercial water electrolysis by novel interfacial engineering.

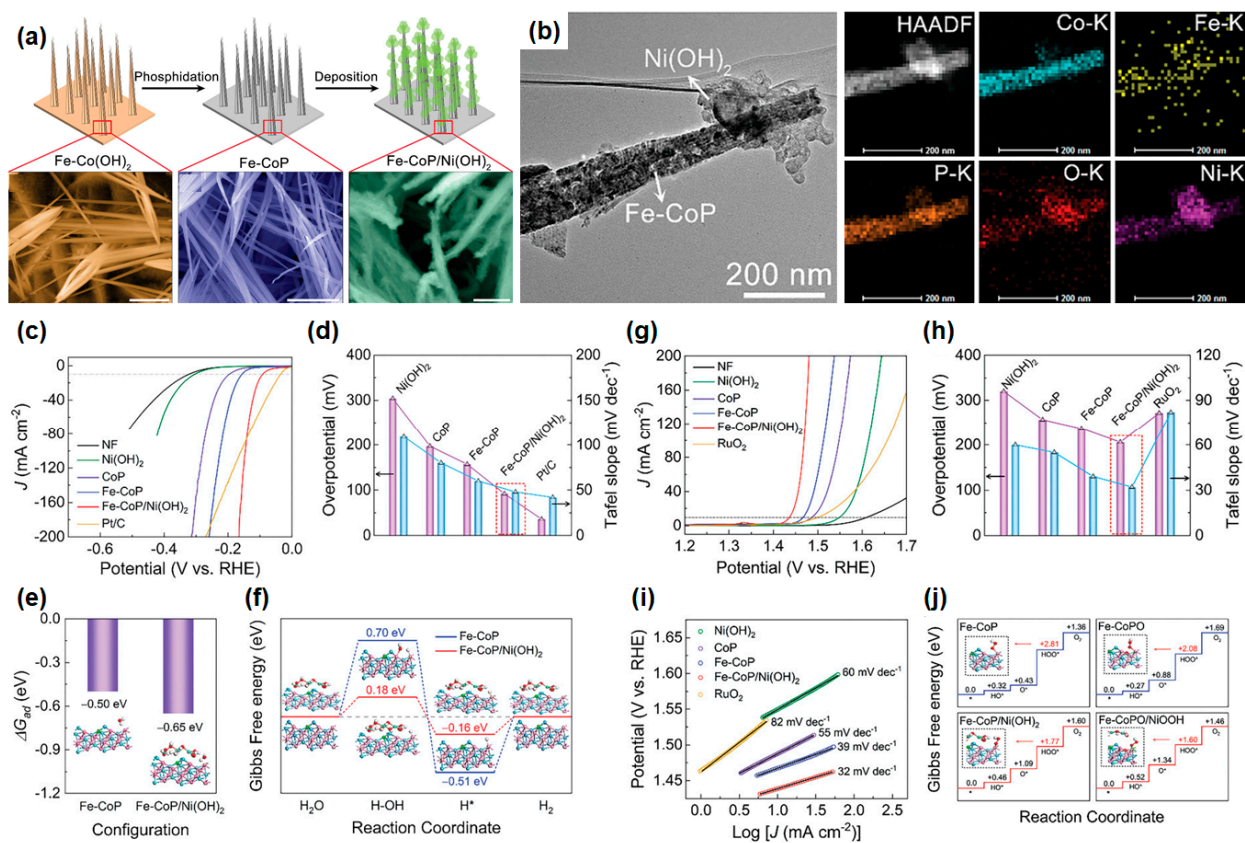


Figure 7. (a) Schematic illustration of the synthesis steps of the Fe-CoP/Ni(OH)₂ hybrid and SEM images of Fe-Co(OH)₂, Fe-CoP, and Fe-CoP/Ni(OH)₂ nanowires. (b) TEM image, HAADF-STEM image, and EDS mapping images of the Fe-CoP/Ni(OH)₂ hybrid nanowire. (c) The iR-corrected LSV curves and (d) comparison of overpotential and Tafel slope at different electrodes for HER in 1 M KOH. (e) Comparison of calculated water adsorption energy (ΔG_{ad}) and (f) calculated Gibbs free energy diagrams for alkaline HER at the bare Fe-CoP surface and the Fe-CoP/Ni(OH)₂ hybrid surface. (g) iR-corrected LSV curves, (h) Tafel plots, and (i) comparison of overpotential and Tafel slope at different electrodes for OER in 1 M KOH. (j) Calculated Gibbs free energy diagrams of the OER pathway at the Fe-CoP, Fe-CoP/Ni(OH)₂, Fe-CoPO, and Fe-CoPO/NiOOH surfaces. Reprinted (adapted) from reference [151], copyright (2021) Wiley-VCH GmbH.

3.2.2. Transition Metal Sulfides and Selenides

Transition metal sulfides and selenides (TMSs) are a group of materials that have gained significant attention due to their unique properties and potential applications in fields such as catalysis, energy conversion and storage, and electronics [152,153]. They have high catalytic activity, good conductivity, and high stability and are low cost, making them an attractive alternative to noble metals. TMSs have good electrical conductivity and thermal and chemical stability. However, they often have poor stability in common solvents and can become less conductive at high temperatures or high humidity. The challenges in using TMSs as an efficient water-splitting electrocatalyst include the need for a facile, large-scale synthesis method with specific structures and morphologies, a better understanding of the mechanisms of TMSs in water splitting, and improved stability, especially in alkaline conditions [154,155]. The following section will introduce two examples of TMS-based electrocatalysts with improved catalytic performance and stability in alkaline water splitting.

Zhang et al. presented an interface- and defect-rich cobalt-doped $\text{Ni}_3\text{S}_2/\text{MoS}_2$ (Co-NMS) hybridized nanosheet decorated on a hierarchical carbon framework with carbon nanowire arrays (CA) supported on conducting carbon cloth (CC). The nanosheets were prepared through a two-step process including the hydrothermal growth of the NiMoO_4 phase and the chemical vulcanization of NiMoO_4 at high temperatures. This two-step reaction is crucial in obtaining heterogeneous rich interfaces and small-size discrete MoS_2 and Ni_3S_2 interfaces. The hydrothermally grown Co-doped NiMoO_4 is vertically aligned on the carbon fiber with a height of 500 nm and thickness of around 50 nm. After the vulcanization at 350 °C in Ar/H_2 (95/5 vol%), the highly segregated NiMoO_4 nanosheets turned to $\text{Ni}_3\text{S}_2/\text{MoS}_2$ heterointerfaces with hierarchical morphologies of nanosheets. They employed the fin-tube-like hierarchical carbon framework (CA/CC) to increase anchoring sites and to expose more surface sites, which can accelerate the mass transport (gas bubbles and electrolyte and electron transfer processes), as shown in Figure 8a [156]. From the chemical vapor vulcanization, the more reactive Ni atoms would be diffused out of NiMoO_4 structures and react with sulfur to form Ni_3S_2 particles. More particles could be precipitated out and gradually aggregated into themselves to form large particles as a function of the increase in vulcanization temperature. The aggregation of Ni_3S_2 particles not only destroyed the structure of nanosheets but also constructed rich and tight heterogeneous interfaces. As the vulcanization temperature increased, the diffraction peaks of MoS_2 and Ni_3S_2 in NMS/CC became sharper and stronger in the XRD, indicating the improvement of the crystallinity of MoS_2 and Ni_3S_2 . The interlayer spacings of 0.63 nm and 0.28 nm were observed as corresponding to the (002) plane of 2H- MoS_2 and (110) crystal plane of Ni_3S_2 , indicating that the chemical vapor vulcanization process is suitable for generating a uniform heterogeneous interface. The tight heterointerfaces between Ni_3S_2 and MoS_2 , which are highlighted by the blue dotted line in Figure 8b, can provide bifunctional active sites for the cleavage of water molecules to H^+ and OH^- . There are many lattice defects such as dislocations, distortions, and discontinuous crystal fringes observed. These defect sites also could play the role of additional catalytic active sites for water splitting.

In the electrochemical characteristics, they conducted a variety of measurements using Ni_3S_2 , MoS_2 , NMS, and Co-doped NMS electrocatalysts on CC and CA substrates to investigate the effect of heterogeneous interface engineering, element doping, electrode structure design, and morphology control. By the heterogeneous interface engineering, the overpotential (η_{10}) of the $\text{Ni}_3\text{S}_2/\text{MoS}_2$ heterostructure exhibited 146 mV at 10 mA/cm^2 , which was reduced by about 100 mV to those of one-component $\text{Ni}_3\text{S}_2/\text{CC}$ ($\eta_{10} = 253$ mV) and MoS_2/CC ($\eta_{10} = 237$ mV). The Co-NMS/CC sample showed a lower overpotential of 115 mV at 10 mA/cm^2 , and that of the Co-NMS/CA samples further decreased to 89 mV (Co-NMS/CA), which was attributed to the hierarchical carbon framework with carbon nanowire arrays, as displayed in Figure 8c. The heterointerface engineering is the most critical strategy among them, by the synergistic fast HER kinetics enabled by two components, which are Ni_3S_2 , which acts as a water dissociation promoter, and

MoS₂, which acts as a hydrogen adsorption active site. In the Tafel slope, as shown in Figure 8d, the Ni₃S₂/CC sample exhibited a low Tafel slope value of 87 mV/dec, which was a remarkably reduced value compared with those of MoS₂/CC (146 mV/dec) and Ni₃S₂/CC (191 mV/dec). The fastest HER kinetics in this study was observed in the Co-NMS/CC sample (62 mV/dec), which meant the interface engineering could be the most effective way to optimize the dynamic approach of HER in an alkaline solution with the largest decrease in the Tafel slope. They compared the Co-NMS/CA electrodes with the previously reported MoS₂-based electrocatalysts in alkaline media, as shown in Figure 8e, indicating that the proposed facile strategies are effective to improve the catalytic activity of MoS₂. Stability is another important factor to determine the efficiency of the electrocatalyst. They conducted the cyclic test and chronopotentiometry measurement at various current densities. There was a slight negative shift after 1000 CV cycles, but no obvious negative voltage shifts were found in chronopotentiometry at 10, 50, and 100 mA/cm² over 50 h. This improved stability might come from the enhanced mass transport and electron transfer processes by 3D hierarchical hole structures. Furthermore, the Co-NMS/CA electrode was coupled with the NiFe LDH/CC anode to evaluate the overall water-splitting performance. The cell potential of the NiFe LDH/CC || Co-NMS/CA system is only 1.66 V at a current density of 10 mA/cm², which is close to that of the NiFe LDH/CC || Pt plate system and durably operated over 10 h in alkaline media. The proposed strategy is an effective way to maximize the heterointerfaces for sulfide-based catalysts and is possibly applied to the synthesis of other heterostructures for various research fields.

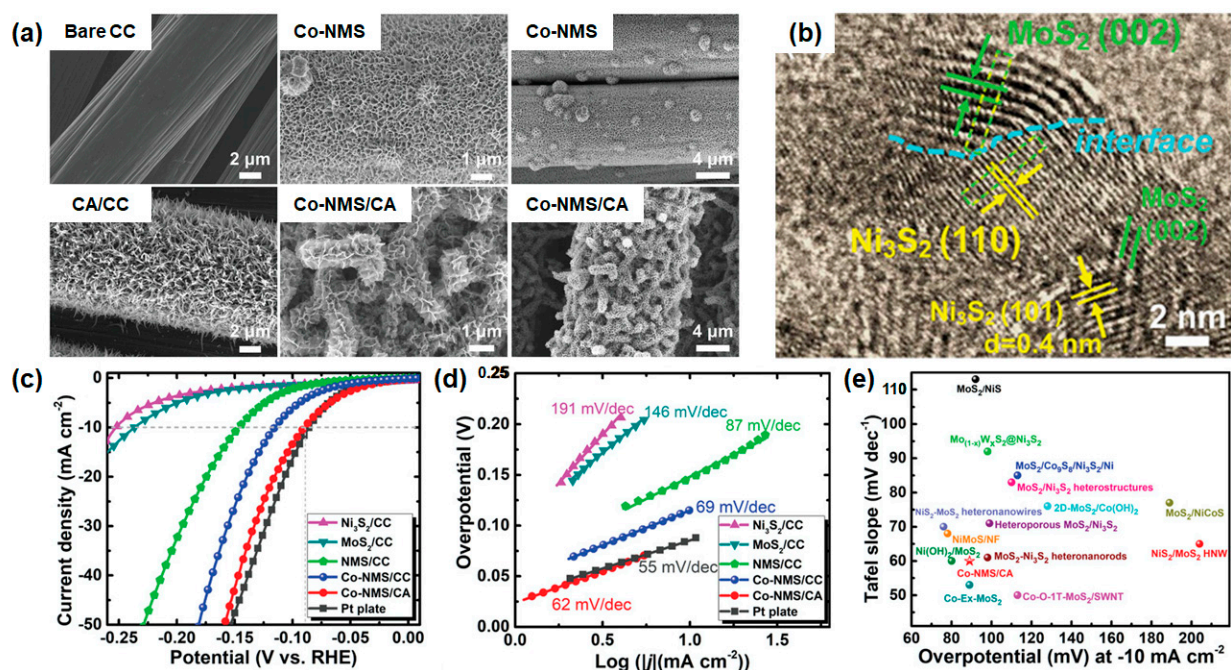


Figure 8. (a) SEM images of bare CC, Co-NMS/CC, CA/CC, and Co-NMS/CA. (b) HRTEM image of Co-NMS. (c) LSV curves of HER for various electrocatalyst samples and (d) corresponding Tafel slopes. (e) Comparison of the overpotential at -10 mA/cm^2 and Tafel slope on various representative MoS₂-based HER electrocatalysts in alkaline electrolyte. Reprinted (adapted) from reference [156], copyright (2021) Wiley-VCH GmbH.

Liu et al. fabricated bimetallic NiFe-based heterostructure nanosheets, consisting of both amorphous NiFe(OH)_x and crystalline (Ni, Fe)Se₂ to improve the OER performance via heterointerface engineering [138]. The interface engineering modulates the electron configuration of the catalysts, resulting in enhanced electron conductivity and favorable free energies at the surface. In Figure 9a, the schematic illustration of the multistep synthesis of NiFe(OH)_x/(Ni, Fe)Se₂ on carbon cloth is provided. NiFe-LDH nanosheets were

synthesized by the hydrothermal method followed by selenization converting them into $(\text{Ni, Fe})\text{Se}_2/\text{CC}$. Then, a core-shell structure of $\text{NiFe}(\text{OH})_x/(\text{Ni, Fe})\text{Se}_2$ was obtained via electrodeposition. In Figure 9b, the SEM image shows the thinly flocculent $\text{NiFe}(\text{OH})_x$ layer coated on the surface of the $(\text{Ni, Fe})\text{Se}_2$ nanosheets. Figure 9f shows the clear lattice fringe with an interplanar spacing of 0.265 corresponding to pyrite $(\text{Ni, Fe})\text{Se}_2$. In Figure 9e, the heterostructured $\text{NiFe}(\text{OH})_x/(\text{Ni, Fe})\text{Se}_2$ electrocatalyst exhibits excellent electrochemical OER performance with considerably low overpotentials of 180, 220, and 230 mV to achieve the current densities of 10, 100, and 300 mA cm^{-2} , which are much lower than those of other electrocatalysts. Furthermore, the as-synthesized catalyst shows the Tafel slope of 42 mV dec^{-1} in Figure 9f, indicating a highly fast surface kinetics. In Figure 9g, compared with the commercial IrO_2 , RuO_2 , and recently reported OER electrocatalysts, $\text{NiFe}(\text{OH})_x/(\text{Ni, Fe})\text{Se}_2$ shows the lowest overpotential and Tafel slope. The authors also conducted the DFT calculation to understand the enhanced catalytic activity derived from the heterointerface between NiFeOOH and $(\text{Ni, Fe})\text{Se}_2$. In Figure 9f, the (110) facet of NiFeOOH and the (100) facet of $(\text{Ni, Fe})\text{Se}_2$ were selected considering a small interfacial strain (0.54%). The differential charge densities described in Figure 9g show that the Ni at the heterointerface has a higher chemical valence since the charge density of the Ni atom is reduced, leading to highly enhanced catalytic activity. In addition, the Gibbs energy profiles of both NiFeOOH and $\text{NiFeOOH}/(\text{Ni, Fe})\text{Se}_2$ suggest that the overpotential (0.98 V) in the rate-determining step ($^*\text{O} \rightarrow ^*\text{OOH}$) of the heterostructure is much lower than that (1.1 V) in the rate-determining step ($^*\text{OH} \rightarrow ^*\text{O}$) of NiFeOOH . This study not only suggested a rational design of amorphous-crystalline bimetallic heterostructures but also revealed their modified electronic coupling and their surface free energies.

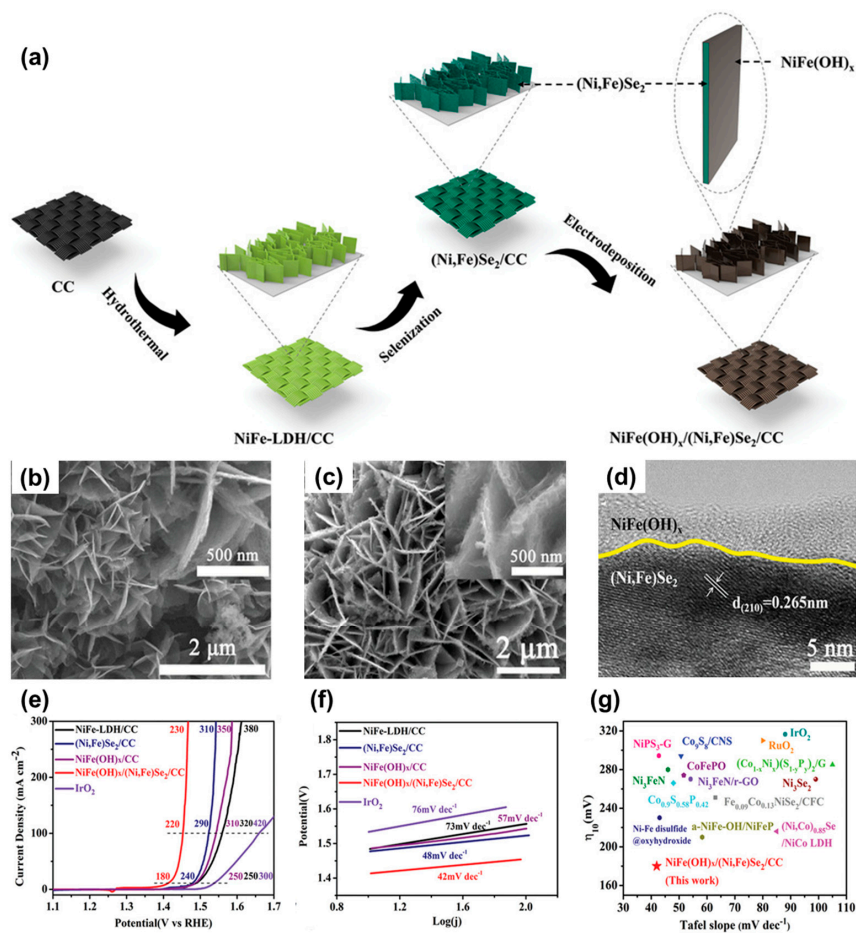


Figure 9. (a) Schematic illustration of the synthesis of $\text{NiFe}(\text{OH})_x/(\text{Ni, Fe})\text{Se}_2$ on carbon cloth. SEM images of (b) $(\text{Ni, Fe})\text{Se}_2/\text{CC}$, (c) $\text{NiFe}(\text{OH})_x/(\text{Ni, Fe})\text{Se}_2/\text{CC}$, and (d) HRTEM images of

NiFe(OH)_x/(Ni, Fe)Se₂/CC. (e) LSV curves and (f) Tafel plots of IrO₂/CC, NiFe-LDH/CC, (Ni, Fe)Se₂/CC, NiFe(OH)_x/CC, and NiFe(OH)_x/(Ni, Fe)Se₂/CC. (g) Overpotential required at 10 mA/cm² (η_{10}) and Tafel slope comparison of the catalysts in this work with other reported high-performance OER electrocatalysts. Reprinted (adapted) from reference [138], copyright (2021) Wiley-VCH GmbH.

3.2.3. Transition Metal Carbides and Nitrides

Transition metal carbides (TMCs) and nitrides (TMNs) are interstitial compounds that embed carbon and nitrogen atoms into the interstitial sites of parent metals. These materials are unique in that they possess a combination of metallic, covalent, and ionic properties that make them ideal for various applications. They offer several beneficial properties including high electrical conductivity, hardness, corrosion resistance, thermal stability, and catalytic activity. These properties are advantageous for electrochemical water splitting. Although several TMCs and TMNs have shown promising performances, it is necessary to improve the limited surface area and difficulty in synthesis.

Yao et al. synthesized porous Cr-doped Co₄N nanorods on carbon cloth and investigated their extraordinary electrocatalytic performance toward alkaline HER [157]. The Cr-doped Co₄N/CC nanorod arrays were synthesized by annealing hydrothermally grown Cr-Co(OH)F with urea at 400 °C in N₂ atmosphere. According to calculations with DFT and experimental results, it has been found that Cr atoms serve as sites for increasing water adsorption and dissociation and also modify the electronic structure of Co₄N to enhance the hydrogen-binding capabilities of Co atoms. This leads to an acceleration in the kinetics of both the alkaline Volmer and Heyrovsky reactions. Interestingly, this approach can be applied to other metals, such as Mo, Mn, and Fe.

Diao et al. successfully synthesized heterostructured W₂N/WC electrocatalysts to reveal the synergistic effect of the heterointerface between W₂N and WC facilitating charge transport and separation [158]. In this research, a facile solid-state synthesis method was adapted to control the interface of the catalysts. Specifically, the porcelain boat containing blue WO₃ powder and dicyandiamide was heated under an Ar atmosphere at 800 °C. In this condition, the W₂N/WC heterostructure with abundant interfaces was obtained. Using DFT calculations and XAFS analysis, it was revealed that the charge density rearrangement occurred at the heterointerface, and C atoms near the interface accepted more electrons from the W atoms, resulting in electron transfer from W₂N to WC. The resultant W₂N/WC showed a high catalytic activity in both HER and OER with a low overpotential of 148.5 and 320 mV at 10 mA/cm².

4. Conclusions and Outlook

Water electrolysis in alkaline conditions for AEMWE is considered the most suitable and advantageous technique for generating hydrogen energy due to the cost-effective electrocatalysts, high current density, and long-term stability. The efficacy of hydrogen generation is significantly related to the productivity of the two half-cell reactions (OER and HER) in water splitting. To minimize the overpotential required for each reaction and operate for a long time, it is critical to design highly active and robust electrocatalysts. In this respect, transition metal oxide/hydroxide-based derivatives have shown great potential since they possess a large surface area, accessible surface atoms, and tunable electronic structure. However, they have limitations in terms of low electrical conductivity and intrinsic active sites.

In this review, we summarize the superiorities of multicomponent electrocatalysts achieved by heterostructure engineering, doping, and single-atom catalysts. Heterostructure engineering induces the formation of defects and modulation of electronic configurations, leading to enhanced charge transfer and lowered surface energy. Additionally, heteroatom doping adjusts the physicochemical properties of oxide/hydroxide-based materials by modifying the morphology and acting as an electron-accepting site. Specifically, the electronic structure of metal ions in metal hydroxides is affected by the electron-deficient

d-orbitals of dopants, enhancing the catalytic activity of multicomponent hydroxides. Finally, the distinct local electronic structure and coordination environment of SACs, with high atomic utilization efficiency, enables the activation of the reactants by modulating the surface energy of single-atomic sites.

Until now, a variety of oxide/hydroxide derivatives have been developed and applied to HER and OER catalysts. Among them, we have covered transition metal oxides, hydroxides, phosphides, sulfides, and selenides, to which heterostructure engineering, doping, and SACs were applied. Many researchers have strengthened the potential of oxide/hydroxide derivatives for practical utilization as electrocatalysts in the AEMWE system. Despite significant progress, there are still some issues that must be addressed for the further advance of oxide/hydroxide-based materials. We highlight three major challenges that oxides/hydroxides face.

1. First, oxides exhibit high durability but relatively low activity due to their highly crystalline phase and chemical stability. Hydroxides are a rising candidate with the highest activity owing to their large electrochemically active surface area, but they still suffer from low electrical conductivity. The main purposes of designing multicomponents are to increase the intrinsic activity, expose more active sites, and accelerate the electron and mass charge kinetics, improving conductivity and electrochemical performances. Thus, the innovative design and synthesis of unique nanostructures are still a great challenge in water splitting.
2. Second, the functional roles of the active sites in oxides/hydroxides structures are not entirely clear. The nanostructured electrocatalysts undergo composition and structural transformations during the reaction under water splitting. Therefore, a deep understanding of the structural transformation is required to determine the real active phases and sites. Gaining insight into the detailed mechanism and structural transformation is critical for predicting the interaction between structure and active sites for high electrical performance in alkaline media.
3. Finally, commercializing and simplifying the water-splitting system on a large scale needs to be further investigated to be optimized. The development of bifunctional electrocatalysis is the key factor that is active for both HER and OER reactions in the same electrolytes. Transition metal oxides/hydroxides have been reported as promising catalysts for the OER process by supporting appropriate bonding strength with adsorbed oxygen intermediates in the water-splitting process, but some catalysts are inactive in HER.

In summary, the use of oxide/hydroxide-based electrocatalysts for AEMWE has shown great potential for hydrogen production. However, there are still challenges that need to be addressed, including increasing intrinsic activity, understanding the role of active sites, and developing bifunctional electrocatalysts for both HER and OER reactions. To achieve these goals, innovative design and synthesis of unique nanostructures, a deeper understanding of the structural transformations and interactions between the structure and active sites, and the optimization of large-scale water-splitting systems are needed. Despite the challenges, the use of oxide/hydroxide-based electrocatalysts remains a promising avenue for sustainable and cost-effective hydrogen production.

Author Contributions: Conceptualization, G.L., S.E.J., S.H.P. and K.C.K.; writing—original draft preparation, G.L., S.E.J., Y.K., I.-H.P., H.W.J., S.H.P. and K.C.K.; writing—review and editing, G.L., S.E.J., Y.K., I.-H.P., H.W.J., S.H.P. and K.C.K.; supervision, S.H.P. and K.C.K.; project administration, K.C.K.; funding acquisition, S.H.P. and K.C.K. All authors have read and agreed to the published version of the manuscript.

Funding: This research was supported by the National Center for Materials Research Data (NCMRD) through the National Research Foundation of Korea (NRF) funded by the Ministry of Science and ICT (NRF-2021M3A7C2089748) and also supported by the KRISS (Korea Research Institute of Standards and Science) MPI Lab Program.

Institutional Review Board Statement: Not applicable.

Informed Consent Statement: Not applicable.

Data Availability Statement: Not applicable.

Acknowledgments: Ki Chang Kwon acknowledges the Characterization platform for advanced materials funded by the Korea Research Institute of Standards and Science (KRISS—2023—GP2023-0014).

Conflicts of Interest: The authors declare no conflict of interest.

References

1. Lewis, N.S.; Nocera, D.G. Powering the Planet: Chemical Challenges in Solar Energy Utilization. *Proc. Natl. Acad. Sci. USA* **2006**, *103*, 15729–15735. [[CrossRef](#)] [[PubMed](#)]
2. Cook, T.R.; Dogutan, D.K.; Reece, S.Y.; Surendranath, Y.; Teets, T.S.; Nocera, D.G. Solar Energy Supply and Storage for the Legacy and Nonlegacy Worlds. *Chem. Rev.* **2010**, *110*, 6474–6502. [[CrossRef](#)] [[PubMed](#)]
3. Vagin, M.; Ivanov, I.G.; Yakimova, R.; Shteplyuk, I. Bidirectional Hydrogen Electrocatalysis on Epitaxial Graphene. *ACS Omega* **2022**, *7*, 13221–13227. [[CrossRef](#)] [[PubMed](#)]
4. Chu, S.; Majumdar, A. Opportunities and Challenges for a Sustainable Energy Future. *Nature* **2012**, *488*, 294–303. [[CrossRef](#)]
5. Zhang, Q.; Tong, Y.; Wang, Z.; Jing, B.; Zhu, Y.; Qiu, S.; Cui, C.; Deng, F. Improved Alkaline Water Electrolysis System for Green Energy: Sulfonamide Antibiotic-Assisted Anodic Oxidation Integrated with Hydrogen Generation. *J. Mater. Chem. A* **2023**, *11*, 6129–6143. [[CrossRef](#)]
6. Zada, A.; Khan, M.; Qureshi, M.N.; Liu, S.Y.; Wang, R. Accelerating Photocatalytic Hydrogen Production and Pollutant Degradation by Functionalizing G-C₃N₄ With SnO₂. *Front. Chem.* **2020**, *7*, 941. [[CrossRef](#)]
7. Hoang, A.L.; Balakrishnan, S.; Hodges, A.; Tsekouras, G.; Al-Musawi, A.; Wagner, K.; Lee, C.Y.; Swiegers, G.F.; Wallace, G.G. High-Performing Catalysts for Energy-Efficient Commercial Alkaline Water Electrolysis. *Sustain. Energy Fuels* **2022**, *7*, 31–60. [[CrossRef](#)]
8. Muthurasu, A.; Chhetri, K.; Dahal, B.; Kim, H.Y. Ruthenium Nanoparticles Integrated Bimetallic Metal-Organic Framework Electrocatalysts for Multifunctional Electrode Materials and Practical Water Electrolysis in Seawater. *Nanoscale* **2022**, *14*, 6557–6569. [[CrossRef](#)]
9. Diao, J.; Li, X.; Wang, S.; Zhao, Z.; Wang, W.; Chen, K.; Chen, X.; Chao, T.; Yang, Y. Promoting Water Splitting on Arrayed Molybdenum Carbide Nanosheets with Electronic Modulation. *J. Mater. Chem. A* **2021**, *9*, 21440–21447. [[CrossRef](#)]
10. Li, Y.; Yin, Z.; Cui, M.; Liu, X.; Xiong, J.; Chen, S.; Ma, T. Interface Engineering of Transitional Metal Sulfide-MoS₂ heterostructure Composites as Effective Electrocatalysts for Water-Splitting. *J. Mater. Chem. A* **2021**, *9*, 2070–2092. [[CrossRef](#)]
11. Liang, C.; Zou, P.; Nairan, A.; Zhang, Y.; Liu, J.; Liu, K.; Hu, S.; Kang, F.; Fan, H.J.; Yang, C. Exceptional Performance of Hierarchical Ni-Fe Oxyhydroxide@NiFe Alloy Nanowire Array Electrocatalysts for Large Current Density Water Splitting. *Energy Environ. Sci.* **2020**, *13*, 86–95. [[CrossRef](#)]
12. Sun, H.; Lian, Y.; Yang, C.; Xiong, L.; Qi, P.; Mu, Q.; Zhao, X.; Guo, J.; Deng, Z.; Peng, Y. A Hierarchical Nickel-Carbon Structure Templated by Metal-Organic Frameworks for Efficient Overall Water Splitting. *Energy Environ. Sci.* **2018**, *11*, 2363–2371. [[CrossRef](#)]
13. Feng, Y.; Guan, Y.; Zhou, E.; Zhang, X.; Wang, Y. Nanoscale Double-Heterojunctional Electrocatalyst for Hydrogen Evolution. *Adv. Sci.* **2022**, *9*, 2201339. [[CrossRef](#)]
14. Shiva Kumar, S.; Himabindu, V. Hydrogen Production by PEM Water Electrolysis—A Review. *Mater. Sci. Energy Technol.* **2019**, *2*, 442–454. [[CrossRef](#)]
15. Vincent, I.; Bessarabov, D. Low Cost Hydrogen Production by Anion Exchange Membrane Electrolysis: A Review. *Renew. Sustain. Energy Rev.* **2018**, *81*, 1690–1704. [[CrossRef](#)]
16. Li, D.; Motz, A.R.; Bae, C.; Fujimoto, C.; Yang, G.; Zhang, F.Y.; Ayers, K.E.; Kim, Y.S. Durability of Anion Exchange Membrane Water Electrolyzers. *Energy Environ. Sci.* **2021**, *14*, 3393–3419. [[CrossRef](#)]
17. Anantharaj, S.; Noda, S.; Jothi, V.R.; Yi, S.C.; Driess, M.; Menezes, P.W. Strategies and Perspectives to Catch the Missing Pieces in Energy-Efficient Hydrogen Evolution Reaction in Alkaline Media. *Angew. Chem. Int. Ed.* **2021**, *60*, 18981–19006. [[CrossRef](#)]
18. Lee, S.A.; Kim, J.; Kwon, K.C.; Park, S.H.; Jang, H.W. Anion Exchange Membrane Water Electrolysis for Sustainable Large-scale Hydrogen Production. *Carbon Neutralization* **2022**, *1*, 26–48. [[CrossRef](#)]
19. Gao, J.; Tao, H.; Liu, B. Progress of Nonprecious-Metal-Based Electrocatalysts for Oxygen Evolution in Acidic Media. *Adv. Mater.* **2021**, *33*, 2003786. [[CrossRef](#)]
20. Park, S.H.; To, D.T.; Myung, N.V. A Review of Nickel-Molybdenum Based Hydrogen Evolution Electrocatalysts from Theory to Experiment. *Appl. Catal. A Gen.* **2023**, *651*, 119013. [[CrossRef](#)]
21. Kwon, H.R.; Park, H.; Jun, S.E.; Choi, S.; Jang, H.W. High Performance Transition Metal-Based Electrocatalysts for Green Hydrogen Production. *Chem. Commun.* **2022**, *58*, 7874–7889. [[CrossRef](#)] [[PubMed](#)]
22. Jun, S.E.; Lee, J.K.; Jang, H.W. Two-Dimensional Materials for Photoelectrochemical Water Splitting. *Energy Adv.* **2023**, *2*, 34–53. [[CrossRef](#)]
23. Xie, Y.; Yu, C.; Ni, L.; Yu, J.; Zhang, Y.; Qiu, J. Carbon-hybridized Hydroxides for Energy Conversion and Storage: Interface Chemistry and Manufacturing. *Adv. Mater.* **2022**, *35*, 2209652. [[CrossRef](#)] [[PubMed](#)]

24. Klingenhof, M.; Hauke, P.; Kroschel, M.; Wang, X.; Merzdorf, T.; Binninger, C.; Ngo Thanh, T.; Paul, B.; Teschner, D.; Schlögl, R.; et al. Anion-Tuned Layered Double Hydroxide Anodes for Anion Exchange Membrane Water Electrolyzers: From Catalyst Screening to Single-Cell Performance. *ACS Energy Lett.* **2022**, *7*, 3415–3422. [[CrossRef](#)]
25. Wu, Z.P.; Caracciolo, D.T.; Maswadeh, Y.; Wen, J.; Kong, Z.; Shan, S.; Vargas, J.A.; Yan, S.; Hopkins, E.; Park, K.; et al. Alloying–Realloying Enabled High Durability for Pt–Pd-3d-Transition Metal Nanoparticle Fuel Cell Catalysts. *Nat. Commun.* **2021**, *12*, 859. [[CrossRef](#)]
26. Dong, J.; Zhang, X.; Huang, J.; Hu, J.; Chen, Z.; Lai, Y. In-Situ Formation of Unsaturated Defect Sites on Converted CoNi Alloy/Co-Ni LDH to Activate MoS₂ Nanosheets for PH-Universal Hydrogen Evolution Reaction. *Chem. Eng. J.* **2021**, *412*, 128556. [[CrossRef](#)]
27. Wang, Y.; Lv, H.; Sun, L.; Liu, B. Mesoporous Noble Metal-Metalloid/Nonmetal Alloy Nanomaterials: Designing Highly Efficient Catalysts. *ACS Nano* **2021**, *15*, 18661–18670. [[CrossRef](#)]
28. Liu, T.; Ma, X.; Liu, D.; Hao, S.; Du, G.; Ma, Y.; Asiri, A.M.; Sun, X.; Chen, L. Mn Doping of CoP Nanosheets Array: An Efficient Electrocatalyst for Hydrogen Evolution Reaction with Enhanced Activity at All PH Values. *ACS Catal.* **2017**, *7*, 98–102. [[CrossRef](#)]
29. Rao, Y.; Chen, S.; Yue, Q.; Kang, Y. Optimizing the Spin States of Mesoporous Co₃O₄ Nanorods through Vanadium Doping for Long-Lasting and Flexible Rechargeable Zn-Air Batteries. *ACS Catal.* **2021**, *11*, 8097–8103. [[CrossRef](#)]
30. Lu, B.A.; Shen, L.F.; Liu, J.; Zhang, Q.; Wan, L.Y.; Morris, D.J.; Wang, R.X.; Zhou, Z.Y.; Li, G.; Sheng, T.; et al. Structurally Disordered Phosphorus-Doped Pt as a Highly Active Electrocatalyst for an Oxygen Reduction Reaction. *ACS Catal.* **2021**, *11*, 355–363. [[CrossRef](#)]
31. Lau, T.H.M.; Wu, S.; Kato, R.; Wu, T.S.; Kulhavý, J.; Mo, J.; Zheng, J.; Foord, J.S.; Soo, Y.L.; Suenaga, K.; et al. Engineering Monolayer 1T-MoS₂ into a Bifunctional Electrocatalyst via Sonochemical Doping of Isolated Transition Metal Atoms. *ACS Catal.* **2019**, *9*, 7527–7534. [[CrossRef](#)]
32. Yang, X.; Wang, A.; Qiao, B.; Li, J.U.N. Single-Atom Catalysts: A New Frontier in heterogeneous catalysis. *Acc. Chem. Res.* **2013**, *46*, 1740–1748. [[CrossRef](#)]
33. Fu, J.; Dong, J.; Si, R.; Sun, K.; Zhang, J.; Li, M.; Yu, N.; Zhang, B.; Humphrey, M.G.; Fu, Q.; et al. Synergistic Effects for Enhanced Catalysis in a Dual Single-Atom Catalyst. *ACS Catal.* **2021**, *11*, 1952–1961. [[CrossRef](#)]
34. Zhai, P.; Xia, M.; Wu, Y.; Zhang, G.; Gao, J.; Zhang, B.; Cao, S.; Zhang, Y.; Li, Z.; Fan, Z.; et al. Engineering Single-Atomic Ruthenium Catalytic Sites on Defective Nickel-Iron Layered Double Hydroxide for Overall Water Splitting. *Nat. Commun.* **2021**, *12*, 4587. [[CrossRef](#)]
35. Zhu, F.; Sun, L.; Liu, Y.; Shi, W. Dual-Defect Site Regulation on MOF-Derived P-Co₃O₄@NC@Ov-NiMnLDH Carbon Arrays for High-Performance Supercapacitors. *J. Mater. Chem. A* **2022**, *10*, 21021–21030. [[CrossRef](#)]
36. Liang, H.; Lin, J.; Jia, H.; Chen, S.; Qi, J.; Cao, J.; Lin, T.; Fei, W.; Feng, J. Hierarchical NiCo-LDH/NiCoP@NiMn-LDH Hybrid Electrodes on Carbon Cloth for Excellent Supercapacitors. *J. Mater. Chem. A* **2018**, *6*, 15040–15046. [[CrossRef](#)]
37. Dennler, G.; Chmielowski, R.; Jacob, S.; Capet, F.; Roussel, P.; Zastrow, S.; Nielsch, K.; Opahle, I.; Madsen, G.K.H. Are Binary Copper Sulfides/Selenides Really New and Promising Thermoelectric Materials? *Adv. Energy Mater.* **2014**, *4*, 1301581. [[CrossRef](#)]
38. He, Y.; Day, T.; Zhang, T.; Liu, H.; Shi, X.; Chen, L.; Snyder, G.J. High Thermoelectric Performance in Non-Toxic Earth-Abundant Copper Sulfide. *Adv. Mater.* **2014**, *26*, 3974–3978. [[CrossRef](#)]
39. Chang Kwon, K.; Choi, S.; Lee, J.; Hong, K.; Sohn, W.; Andoshe, D.M.; Choi, K.S.; Kim, Y.; Han, S.; Kim, S.Y.; et al. Drastically Enhanced Hydrogen Evolution Activity by 2D to 3D Structural Transition in Anion-Engineered Molybdenum Disulfide Thin Films for Efficient Si-Based Water Splitting Photocathodes. *J. Mater. Chem. A* **2017**, *5*, 15534–15542. [[CrossRef](#)]
40. Kou, Z.; Wang, T.; Gu, Q.; Xiong, M.; Zheng, L.; Li, X.; Pan, Z.; Chen, H.; Verpoort, F.; Cheetham, A.K.; et al. Rational Design of Holey 2D Nonlayered Transition Metal Carbide/Nitride Heterostructure Nanosheets for Highly Efficient Water Oxidation. *Adv. Energy Mater.* **2019**, *9*, 1803768. [[CrossRef](#)]
41. Chen, P.; Ye, J.; Wang, H.; Ouyang, L.; Zhu, M. Recent Progress of Transition Metal Carbides/Nitrides for Electrocatalytic Water Splitting. *J. Alloys Compd.* **2021**, *883*, 160833. [[CrossRef](#)]
42. Liu, S.; Cao, E.; Chen, Z.; Wu, H.; Liu, B.; Yang, J.; Du, S.; Ren, Z. Promoting Electrocatalytic Oxygen Evolution of Ultrasmall NiFe (Hydr)Oxide Nanoparticles by Graphene-Support Effects. *ChemSusChem* **2021**, *14*, 5508–5516. [[CrossRef](#)] [[PubMed](#)]
43. Tang, Y.; Jia, X.; Guo, Y.; Geng, Z.; Wang, C.; Liu, L.; Zhang, J.; Guo, W.; Tan, X.; Yu, T.; et al. Surface Unsaturated Sulfur Modulates Pt Sub-Nanoparticles on Tandem Homo Junction CdS for Efficient Electron Extraction. *Adv. Energy Mater.* **2023**, *13*, 2203827. [[CrossRef](#)]
44. Chen, P.; Xu, K.; Zhou, T.; Tong, Y.; Wu, J.; Cheng, H.; Lu, X.; Ding, H.; Wu, C.; Xie, Y. Strong-Coupled Cobalt Borate Nanosheets/Graphene Hybrid as Electrocatalyst for Water Oxidation under Both Alkaline and Neutral Conditions. *Angew. Chem. Int. Ed.* **2016**, *55*, 2488–2492. [[CrossRef](#)]
45. Momeni, S.; Ghorbani-Vaghei, R. Synthesis, Properties, and Application of the New Nanocatalyst of Double Layer Hydroxides in the One-Pot Multicomponent Synthesis of 2-Amino-3-Cyanopyridine Derivatives. *Sci. Rep.* **2023**, *13*, 1627. [[CrossRef](#)]
46. Kim, B.; Kim, T.; Lee, K.; Li, J. Recent Advances in Transition Metal Phosphide Electrocatalysts for Water Splitting under Neutral PH Conditions. *ChemElectroChem* **2020**, *7*, 3578–3589. [[CrossRef](#)]
47. Jun, S.E.; Kim, Y.H.; Kim, J.; Cheon, W.S.; Choi, S.; Yang, J.; Park, H.; Lee, H.; Park, S.H.; Kwon, K.C.; et al. Atomically Dispersed Iridium Catalysts on Silicon Photoanode for Efficient Photoelectrochemical Water Splitting. *Nat. Commun.* **2023**, *14*, 609. [[CrossRef](#)]

48. Zhang, S.; Nguyen, L.; Liang, J.X.; Shan, J.; Liu, J.J.; Frenkel, A.I.; Patlolla, A.; Huang, W.; Li, J.; Tao, F.F. Catalysis on Singly Dispersed Bimetallic Sites. *Nat. Commun.* **2015**, *6*, 7938. [[CrossRef](#)]
49. Kyriakou, G.; Boucher, M.B.; Jewell, A.D.; Lewis, E.A.; Lawton, T.J.; Baber, A.E.; Tierney, H.L.; Flytzani-stephanopoulos, M.; Sykes, E.C.H. Isolated Metal Atom Geometries as a Strategy for Selective Heterogeneous Hydrogenations. *Science* **2012**, *335*, 1209–1212. [[CrossRef](#)]
50. Yang, S.; Kim, J.; Tak, Y.J.; Soon, A.; Lee, H. Single-Atom Catalyst of Platinum Supported on Titanium Nitride for Selective Electrochemical Reactions. *Angew. Chem. Int. Ed.* **2016**, *55*, 2058–2062. [[CrossRef](#)]
51. Roger, I.; Shipman, M.A.; Symes, M.D. Earth-Abundant Catalysts for Electrochemical and Photoelectrochemical Water Splitting. *Nat. Rev. Chem.* **2017**, *1*, 0003. [[CrossRef](#)]
52. Ilyas, T.; Raziq, F.; Ali, S.; Zada, A.; Ilyas, N.; Shaha, R.; Wang, Y.; Qiao, L. Facile Synthesis of MoS₂/Cu as Trifunctional Catalyst for Electrochemical Overall Water Splitting and Photocatalytic CO₂ Conversion. *Mater. Des.* **2021**, *204*, 109674. [[CrossRef](#)]
53. Yu, J.M.; Lee, J.; Kim, Y.S.; Song, J.; Oh, J.; Lee, S.M.; Jeong, M.; Kim, Y.; Kwak, J.H.; Cho, S.; et al. High-Performance and Stable Photoelectrochemical Water Splitting Cell with Organic-Photoactive-Layer-Based Photoanode. *Nat. Commun.* **2020**, *11*, 5509. [[CrossRef](#)]
54. Wang, S.; Lu, A.; Zhong, C.J. Hydrogen Production from Water Electrolysis: Role of Catalysts. *Nano Converg.* **2021**, *8*, 4. [[CrossRef](#)]
55. Mahmood, N.; Yao, Y.; Zhang, J.W.; Pan, L.; Zhang, X.; Zou, J.J. Electrocatalysts for Hydrogen Evolution in Alkaline Electrolytes: Mechanisms, Challenges, and Prospective Solutions. *Adv. Sci.* **2018**, *5*, 1700464. [[CrossRef](#)]
56. Wei, J.; Zhou, M.; Long, A.; Xue, Y.; Liao, H.; Wei, C.; Xu, Z.J. Heterostructured Electrocatalysts for Hydrogen Evolution Reaction Under Alkaline Conditions. *Nano-Micro Lett.* **2018**, *10*, 75. [[CrossRef](#)]
57. Đurovič, M.; Hnát, J.; Bouzek, K. Electrocatalysts for the Hydrogen Evolution Reaction in Alkaline and Neutral Media. A Comparative Review. *J. Power Sources* **2021**, *493*, 229708. [[CrossRef](#)]
58. Bhalothia, D.; Krishnia, L.; Yang, S.S.; Yan, C.; Hsiung, W.H.; Wang, K.W.; Chen, T.Y. Recent Advancements and Future Prospects of Noble Metal-Based Heterogeneous Nanocatalysts for Oxygen Reduction and Hydrogen Evolution Reactions. *Appl. Sci.* **2020**, *10*, 7708. [[CrossRef](#)]
59. Xie, X.; Du, L.; Yan, L.; Park, S.; Qiu, Y.; Sokolowski, J.; Wang, W.; Shao, Y. Oxygen Evolution Reaction in Alkaline Environment: Material Challenges and Solutions. *Adv. Funct. Mater.* **2022**, *32*, 2110036. [[CrossRef](#)]
60. Liang, Y.; Banjac, K.; Martin, K.; Zigon, N.; Lee, S.; Vanthuyne, N.; Garcés-Pineda, F.A.; Galán-Mascarós, J.R.; Hu, X.; Avarvari, N.; et al. Enhancement of Electrocatalytic Oxygen Evolution by Chiral Molecular Functionalization of Hybrid 2D Electrodes. *Nat. Commun.* **2022**, *13*, 3356. [[CrossRef](#)]
61. Liang, Q.; Brocks, G.; Bieberle-Hütter, A. Oxygen Evolution Reaction (OER) Mechanism under Alkaline and Acidic Conditions. *J. Phys. Energy* **2021**, *3*, 026001. [[CrossRef](#)]
62. Plevová, M.; Hnát, J.; Bouzek, K. Electrocatalysts for the Oxygen Evolution Reaction in Alkaline and Neutral Media. A Comparative Review. *J. Power Sources* **2021**, *507*, 230072. [[CrossRef](#)]
63. Yang, R.; Zhou, Y.; Xing, Y.; Li, D.; Jiang, D.; Chen, M.; Shi, W.; Yuan, S. Synergistic Coupling of CoFe-LDH Arrays with NiFe-LDH Nanosheet for Highly Efficient Overall Water Splitting in Alkaline Media. *Appl. Catal. B Environ.* **2019**, *253*, 131–139. [[CrossRef](#)]
64. Guo, Y.; Park, T.; Yi, J.W.; Henzie, J.; Kim, J.; Wang, Z.; Jiang, B.; Bando, Y.; Sugahara, Y.; Tang, J.; et al. Nanoarchitectonics for Transition-Metal-Sulfide-Based Electrocatalysts for Water Splitting. *Adv. Mater.* **2019**, *31*, e1807134. [[CrossRef](#)] [[PubMed](#)]
65. Sun, H.; Yan, Z.; Liu, F.; Xu, W.; Cheng, F.; Chen, J. Self-Supported Transition-Metal-Based Electrocatalysts for Hydrogen and Oxygen Evolution. *Adv. Mater.* **2020**, *32*, e1806326. [[CrossRef](#)]
66. Han, L.; Dong, S.; Wang, E. Transition-Metal (Co, Ni, and Fe)-Based Electrocatalysts for the Water Oxidation Reaction. *Adv. Mater.* **2016**, *28*, 9266–9291. [[CrossRef](#)]
67. He, Z.; Zhang, J.; Gong, Z.; Lei, H.; Zhou, D.; Zhang, N.; Mai, W.; Zhao, S.; Chen, Y. Activating Lattice Oxygen in NiFe-Based (Oxy)Hydroxide for Water Electrolysis. *Nat. Commun.* **2022**, *13*, 2191. [[CrossRef](#)]
68. Xia, L.; Bo, L.; Shi, W.; Zhang, Y.; Shen, Y.; Ji, X.; Guan, X.; Wang, Y.; Tong, J. Defect and Interface Engineering of Templated Synthesis of Hollow Porous Co₃O₄/CoMoO₄ with Highly Enhanced Electrocatalytic Activity for Oxygen Evolution Reaction. *Chem. Eng. J.* **2023**, *452*, 139250. [[CrossRef](#)]
69. Song, F.; Bai, L.; Moysiadou, A.; Lee, S.; Hu, C.; Liardet, L.; Hu, X. Transition Metal Oxides as Electrocatalysts for the Oxygen Evolution Reaction in Alkaline Solutions: An Application-Inspired Renaissance. *J. Am. Chem. Soc.* **2018**, *140*, 7748–7759. [[CrossRef](#)]
70. Zhang, H.; Maijenburg, A.W.; Li, X.; Schweizer, S.L.; Wehrspohn, R.B. Bifunctional Heterostructured Transition Metal Phosphides for Efficient Electrochemical Water Splitting. *Adv. Funct. Mater.* **2020**, *30*, 2003261. [[CrossRef](#)]
71. Zhu, J.Y.; Xue, Q.; Xue, Y.Y.; Ding, Y.; Li, F.M.; Jin, P.; Chen, P.; Chen, Y. Iridium Nanotubes as Bifunctional Electrocatalysts for Oxygen Evolution and Nitrate Reduction Reactions. *ACS Appl. Mater. Interfaces* **2020**, *12*, 14064–14070. [[CrossRef](#)]
72. Han, J.; Zhang, M.; Bai, X.; Duan, Z.; Tang, T.; Guan, J. Mesoporous Mn-Fe Oxyhydroxides for Oxygen Evolution. *Inorg. Chem. Front.* **2022**, *9*, 3559–3565. [[CrossRef](#)]
73. You, C.; Ji, Y.; Liu, Z.; Xiong, X.; Sun, X. Ultrathin CoFe-Borate Layer Coated CoFe-Layered Double Hydroxide Nanosheets Array: A Non-Noble-Metal 3D Catalyst Electrode for Efficient and Durable Water Oxidation in Potassium Borate. *ACS Sustain. Chem. Eng.* **2018**, *6*, 1527–1531. [[CrossRef](#)]

74. Kwon, K.C.; Suh, J.M.; Varma, R.S.; Shokouhimehr, M.; Jang, H.W. Electrocatalytic Water Splitting and CO₂ Reduction: Sustainable Solutions via Single-Atom Catalysts Supported on 2D Materials. *Small Methods* **2019**, *3*, 201800492. [[CrossRef](#)]
75. Li, Z.; Ma, Q.; Zhang, H.; Zhang, Q.; Zhang, K.; Mei, H.; Xu, B.; Sun, D. Self-Assembly of Metal-Organic Frameworks on Graphene Oxide Nanosheets and In Situ Conversion into a Nickel Hydroxide/Graphene Oxide Battery-Type Electrode. *Inorg. Chem.* **2022**, *61*, 12129–12137. [[CrossRef](#)]
76. Jeon, S.S.; Kang, P.W.; Klingenhof, M.; Lee, H.; Dionigi, F.; Strasser, P. Active Surface Area and Intrinsic Catalytic Oxygen Evolution Reactivity of NiFe LDH at Reactive Electrode Potentials Using Capacitances. *ACS Catal.* **2023**, *13*, 1186–1196. [[CrossRef](#)]
77. Dresp, S.; Dionigi, F.; Klingenhof, M.; Merzdorf, T.; Schmies, H.; Drnec, J.; Poulain, A.; Strasser, P. Molecular Understanding of the Impact of Saline Contaminants and Alkaline PH on NiFe Layered Double Hydroxide Oxygen Evolution Catalysts. *ACS Catal.* **2021**, *11*, 6800–6809. [[CrossRef](#)]
78. Jun, S.E.; Hong, S.P.; Choi, S.; Kim, C.; Ji, S.G.; Park, I.J.; Lee, S.A.; Yang, J.W.; Lee, T.H.; Sohn, W.; et al. Boosting Unassisted Alkaline Solar Water Splitting Using Silicon Photocathode with TiO₂ Nanorods Decorated by Edge-Rich MoS₂ Nanoplates. *Small* **2021**, *17*, 202103457. [[CrossRef](#)]
79. Du, X.; Su, H.; Zhang, X. Metal-Organic Framework-Derived Cu-Doped Co₉S₈ Nanorod Array with Less Low-Valence Co Sites as Highly Efficient Bifunctional Electrodes for Overall Water Splitting. *ACS Sustain. Chem. Eng.* **2019**, *7*, 16917–16926. [[CrossRef](#)]
80. Tran, Y.B.N.; Nguyen, P.T.K.; Luong, Q.T.; Nguyen, K.D. Series of M-MOF-184 (M = Mg, Co, Ni, Zn, Cu, Fe) Metal-Organic Frameworks for Catalysis Cycloaddition of CO₂. *Inorg. Chem.* **2020**, *59*, 16747–16759. [[CrossRef](#)]
81. Jia, L.; Du, G.; Han, D.; Hao, Y.; Zhao, W.; Fan, Y.; Su, Q.; Ding, S.; Xu, B. Ni₃S₂/Cu-NiCo LDH Heterostructure Nanosheet Arrays on Ni Foam for Electrocatalytic Overall Water Splitting. *J. Mater. Chem. A* **2021**, *9*, 27639–27650. [[CrossRef](#)]
82. Han, M.; Wang, C.; Zhong, J.; Han, J.; Wang, N.; Seifitokaldani, A.; Yu, Y.; Liu, Y.; Sun, X.; Vomiero, A.; et al. Promoted Self-Construction of β-NiOOH in Amorphous High Entropy Electrocatalysts for the Oxygen Evolution Reaction. *Appl. Catal. B Environ.* **2022**, *301*, 120764. [[CrossRef](#)]
83. Gao, X.; Zhao, Y.; Dai, K.; Wang, J.; Zhang, B.; Shen, X. NiCoP Nanowire@NiCo-Layered Double Hydroxides Nanosheet Heterostructure for Flexible Asymmetric Supercapacitors. *Chem. Eng. J.* **2020**, *384*, 123373. [[CrossRef](#)]
84. Xiong, P.; Zhang, F.; Zhang, X.; Wang, S.; Liu, H.; Sun, B.; Zhang, J.; Sun, Y.; Ma, R.; Bando, Y.; et al. Strain Engineering of Two-Dimensional Multilayered Heterostructures for beyond-Lithium-Based Rechargeable Batteries. *Nat. Commun.* **2020**, *11*, 3297. [[CrossRef](#)]
85. Wang, S.; Zhao, S.; Guo, X.; Wang, G. 2D Material-Based Heterostructures for Rechargeable Batteries. *Adv. Energy Mater.* **2022**, *12*, 202100864. [[CrossRef](#)]
86. Ilyas, T.; Raziq, F.; Ilyas, N.; Yang, L.; Ali, S.; Zada, A.; Bakhtiar, S.H.; Wang, Y.; Shen, H.; Qiao, L. FeNi@CNS Nanocomposite as an Efficient Electrochemical Catalyst for N₂-to-NH₃ Conversion under Ambient Conditions. *J. Mater. Sci. Technol.* **2022**, *103*, 59–66. [[CrossRef](#)]
87. Zheng, X.; Cui, P.; Qian, Y.; Zhao, G.; Zheng, X.; Xu, X.; Cheng, Z.; Liu, Y.; Dou, S.X.; Sun, W. Multifunctional Active-Center-Transferable Platinum/Lithium Cobalt Oxide Heterostructured Electrocatalysts towards Superior Water Splitting. *Angew. Chem. Int. Ed.* **2020**, *59*, 14533–14540. [[CrossRef](#)]
88. Gong, M.; Zhou, W.; Tsai, M.C.; Zhou, J.; Guan, M.; Lin, M.C.; Zhang, B.; Hu, Y.; Wang, D.Y.; Yang, J.; et al. Nanoscale Nickel Oxide/Nickel Heterostructures for Active Hydrogen Evolution Electrocatalysis. *Nat. Commun.* **2014**, *5*, 4695. [[CrossRef](#)]
89. Hu, W.; Shi, Q.; Chen, Z.; Yin, H.; Zhong, H.; Wang, P. Co₂N/Co₂Mo₃O₈ Heterostructure as a Highly Active Electrocatalyst for an Alkaline Hydrogen Evolution Reaction. *ACS Appl. Mater. Interfaces* **2021**, *13*, 8337–8343. [[CrossRef](#)]
90. Xu, Q.; Zhang, J.; Zhang, H.; Zhang, L.; Chen, L.; Hu, Y.; Jiang, H.; Li, C. Atomic Heterointerface Engineering Overcomes the Activity Limitation of Electrocatalysts and Promises Highly-Efficient Alkaline Water Splitting. *Energy Environ. Sci.* **2021**, *14*, 5228–5259. [[CrossRef](#)]
91. Zada, A.; Khan, M.; Hussain, Z.; Shah, M.I.A.; Ateeq, M.; Ullah, M.; Ali, N.; Shaheen, S.; Yasmeen, H.; Ali Shah, S.N.; et al. Extended Visible Light Driven Photocatalytic Hydrogen Generation by Electron Induction from G-C₃N₄nanosheets to ZnO through the Proper Heterojunction. *Z. Fur Phys. Chem.* **2022**, *236*, 53–66. [[CrossRef](#)]
92. Zhang, A.; Liang, Y.; Zhang, H.; Geng, Z.; Zeng, J. Doping Regulation in Transition Metal Compounds for Electrocatalysis. *Chem. Soc. Rev.* **2021**, *50*, 9817–9844. [[CrossRef](#)]
93. Wang, J.; Liao, T.; Wei, Z.; Sun, J.; Guo, J.; Sun, Z. Heteroatom-Doping of Non-Noble Metal-Based Catalysts for Electrocatalytic Hydrogen Evolution: An Electronic Structure Tuning Strategy. *Small Methods* **2021**, *5*, 2000988. [[CrossRef](#)]
94. Lee, W.J.; Lim, J.; Kim, S.O. Nitrogen Dopants in Carbon Nanomaterials: Defects or a New Opportunity? *Small Methods* **2017**, *1*, 201600014. [[CrossRef](#)]
95. Zhang, J.; Shi, J.; Qi, D.C.; Chen, L.; Zhang, K.H.L. Recent Progress on the Electronic Structure, Defect, and Doping Properties of Ga₂O₃. *APL Mater.* **2020**, *8*, 020906. [[CrossRef](#)]
96. Shin, H.; Xiao, H.; Goddard, W.A. In Silico Discovery of New Dopants for Fe-Doped Ni Oxyhydroxide (Ni_{1-x}Fe_xOOH) Catalysts for Oxygen Evolution Reaction. *J. Am. Chem. Soc.* **2018**, *140*, 6745–6748. [[CrossRef](#)]
97. Xu, H.; Liu, T.; Bai, S.; Li, L.; Zhu, Y.; Wang, J.; Yang, S.; Li, Y.; Shao, Q.; Huang, X. Cation Exchange Strategy to Single-Atom Noble-Metal Doped CuO Nanowire Arrays with Ultralow Overpotential for H₂O Splitting. *Nano Lett.* **2020**, *20*, 5482–5489. [[CrossRef](#)]

98. Jiang, J.; Sun, F.; Zhou, S.; Hu, W.; Zhang, H.; Dong, J.; Jiang, Z.; Zhao, J.; Li, J.; Yan, W.; et al. Atomic-Level Insight into Super-Efficient Electrocatalytic Oxygen Evolution on Iron and Vanadium Co-Doped Nickel (Oxy)Hydroxide. *Nat. Commun.* **2018**, *9*, 2885. [[CrossRef](#)]
99. Wu, J.; Han, N.; Ning, S.; Chen, T.; Zhu, C.; Pan, C.; Wu, H.; Pennycook, S.J.; Guan, C. Single-Atom Tungsten-Doped CoP Nanoarrays as a High-Efficiency PH-Universal Catalyst for Hydrogen Evolution Reaction. *ACS Sustain. Chem. Eng.* **2020**, *8*, 14825–14832. [[CrossRef](#)]
100. Shan, H.; Qin, J.; Wang, J.; Sari, H.M.K.; Lei, L.; Xiao, W.; Li, W.; Xie, C.; Yang, H.; Luo, Y.; et al. Doping-Induced Electronic/Ionic Engineering to Optimize the Redox Kinetics for Potassium Storage: A Case Study of Ni-Doped CoSe₂. *Adv. Sci.* **2022**, *9*, 1–12. [[CrossRef](#)]
101. Qian, G.; Chen, J.; Yu, T.; Luo, L.; Yin, S. N-Doped Graphene-Decorated NiCo Alloy Coupled with Mesoporous NiCoMoO Nano-Sheet Heterojunction for Enhanced Water Electrolysis Activity at High Current Density. *Nano-Micro Lett.* **2021**, *13*, 77. [[CrossRef](#)] [[PubMed](#)]
102. Gao, K.; Wang, B.; Tao, L.; Cuning, B.V.; Zhang, Z.; Wang, S.; Ruoff, R.S.; Qu, L. Efficient Metal-Free Electrocatalysts from N-Doped Carbon Nanomaterials: Mono-Doping and Co-Doping. *Adv. Mater.* **2019**, *31*, e1805121. [[CrossRef](#)] [[PubMed](#)]
103. Liu, Y.; Ye, C.; Zhao, S.N.; Wu, Y.; Liu, C.; Huang, J.; Xue, L.; Sun, J.; Zhang, W.; Wang, X.; et al. A Dual-Site Doping Strategy for Developing Efficient Perovskite Oxide Electrocatalysts towards Oxygen Evolution Reaction. *Nano Energy* **2022**, *99*, 107344. [[CrossRef](#)]
104. Dang Van, C.; Kim, S.; Kim, M.; Lee, M.H. Effect of Rare-Earth Element Doping on NiFe-Layered Double Hydroxides for Water Oxidation at Ultrahigh Current Densities. *ACS Sustain. Chem. Eng.* **2023**, *11*, 1333–1343. [[CrossRef](#)]
105. Ling, T.; Jaroniec, M.; Qiao, S.Z. Recent Progress in Engineering the Atomic and Electronic Structure of Electrocatalysts via Cation Exchange Reactions. *Adv. Mater.* **2020**, *32*, 202001866. [[CrossRef](#)]
106. Yu, F.; Zhou, H.; Huang, Y.; Sun, J.; Qin, F.; Bao, J.; Goddard, W.A.; Chen, S.; Ren, Z. High-Performance Bifunctional Porous Non-Noble Metal Phosphide Catalyst for Overall Water Splitting. *Nat. Commun.* **2018**, *9*, 2551. [[CrossRef](#)]
107. Habibi, R.; Mehrpooya, M.; Ganjali, M. Synthesis of Ternary CoZnAl Layered Double Hydroxide and Co-Embedded N-Doped Carbon Nanotube Hollow Polyhedron Nanocomposite as a Bifunctional Material for ORR Electrocatalyst and Supercapacitor Electrode. *J. Energy Storage* **2022**, *54*, 105377. [[CrossRef](#)]
108. Fan, B.; Wang, H.; Han, X.; Deng, Y.; Hu, W. Single Atoms (Pt, Ir and Rh) Anchored on Activated NiCo LDH for Alkaline Hydrogen Evolution Reaction. *Chem. Commun.* **2022**, *58*, 8254–8257. [[CrossRef](#)]
109. Stephanopoulos, F.; Commu, N. Single Atom Catalysts Push the Boundaries of Heterogeneous Catalysis. *Nat. Commun.* **2021**, *12*, 5884. [[CrossRef](#)]
110. Ji, S.; Chen, Y.; Wang, X.; Zhang, Z.; Wang, D.; Li, Y. Chemical Synthesis of Single Atomic Site Catalysts. *Chem. Rev.* **2020**, *120*, 11900–11955. [[CrossRef](#)]
111. Wang, Y.; Su, H.; He, Y.; Li, L.; Zhu, S.; Shen, H.; Xie, P.; Fu, X.; Zhou, G.; Feng, C.; et al. Advanced Electrocatalysts with Single-Metal-Atom Active Sites. *Chem. Rev.* **2020**, *120*, 12217–12314. [[CrossRef](#)]
112. Wu, L.; Guo, T.; Li, T. Rational Design of Transition Metal Single-Atom Electrocatalysts: A Simulation-Based, Machine Learning-Accelerated Study. *J. Mater. Chem. A* **2020**, *8*, 19290–19299. [[CrossRef](#)]
113. Zheng, J.; Lebedev, K.; Wu, S.; Huang, C.; Ayyvall, T.; Wu, T.S.; Li, Y.; Ho, P.L.; Soo, Y.L.; Kirkland, A.; et al. High Loading of Transition Metal Single Atoms on Chalcogenide Catalysts. *J. Am. Chem. Soc.* **2021**, *143*, 7979–7990. [[CrossRef](#)]
114. Xu, H.; Zhao, Y.; He, G.; Chen, H. Race on Engineering Noble Metal Single-Atom Electrocatalysts for Water Splitting. *Int. J. Hydrogen Energy* **2022**, *47*, 14257–14279. [[CrossRef](#)]
115. Abdelghafar, F.; Xu, X.; Jiang, S.P.; Shao, Z. Designing Single-Atom Catalysts toward Improved Alkaline Hydrogen Evolution Reaction. *Mater. Reports Energy* **2022**, *2*, 100144. [[CrossRef](#)]
116. Fang, S.; Zhu, X.; Liu, X.; Gu, J.; Liu, W.; Wang, D.; Zhang, W.; Lin, Y.; Lu, J.; Wei, S.; et al. Uncovering Near-Free Platinum Single-Atom Dynamics during Electrochemical Hydrogen Evolution Reaction. *Nat. Commun.* **2020**, *11*, 3232. [[CrossRef](#)]
117. Wu, Z.Y.; Karamad, M.; Yong, X.; Huang, Q.; Cullen, D.A.; Zhu, P.; Xia, C.; Xiao, Q.; Shakouri, M.; Chen, F.Y.; et al. Electrochemical Ammonia Synthesis via Nitrate Reduction on Fe Single Atom Catalyst. *Nat. Commun.* **2021**, *12*, 2870. [[CrossRef](#)]
118. Lei, Z.; Cai, W.; Rao, Y.; Wang, K.; Jiang, Y.; Liu, Y.; Jin, X.; Li, J.; Lv, Z.; Jiao, S.; et al. Coordination Modulation of Iridium Single-Atom Catalyst Maximizing Water Oxidation Activity. *Nat. Commun.* **2022**, *13*, 24. [[CrossRef](#)]
119. Qi, K.; Cui, X.; Gu, L.; Yu, S.; Fan, X.; Luo, M.; Xu, S.; Li, N.; Zheng, L.; Zhang, Q.; et al. Single-Atom Cobalt Array Bound to Distorted 1T MoS₂ with Ensemble Effect for Hydrogen Evolution Catalysis. *Nat. Commun.* **2019**, *10*, 5231. [[CrossRef](#)]
120. Shang, H.; Zhou, X.; Dong, J.; Li, A.; Zhao, X.; Liu, Q.; Lin, Y.; Pei, J.; Li, Z.; Jiang, Z.; et al. Engineering Unsymmetrically Coordinated Cu-S1N3 Single Atom Sites with Enhanced Oxygen Reduction Activity. *Nat. Commun.* **2020**, *11*, 3049. [[CrossRef](#)]
121. Liu, K.; Fu, J.; Lin, Y.; Luo, T.; Ni, G.; Li, H.; Lin, Z.; Liu, M. Insights into the Activity of Single-Atom Fe-N-C Catalysts for Oxygen Reduction Reaction. *Nat. Commun.* **2022**, *13*, 2075. [[CrossRef](#)] [[PubMed](#)]
122. Zhang, R.; Jiao, L.; Yang, W.; Wan, G.; Jiang, H.L. Single-Atom Catalysts Templated by Metal-Organic Frameworks for Electrochemical Nitrogen Reduction. *J. Mater. Chem. A* **2019**, *7*, 26371–26377. [[CrossRef](#)]
123. Zang, W.; Yang, T.; Zou, H.; Xi, S.; Zhang, H.; Liu, X.; Kou, Z.; Du, Y.; Feng, Y.P.; Shen, L.; et al. Copper Single Atoms Anchored in Porous Nitrogen-Doped Carbon as Efficient PH-Universal Catalysts for the Nitrogen Reduction Reaction. *ACS Catal.* **2019**, *9*, 10166–10173. [[CrossRef](#)]

124. Yang, H.; Wu, Y.; Li, G.; Lin, Q.; Hu, Q.; Zhang, Q.; Liu, J.; He, C. Scalable Production of Efficient Single-Atom Copper Decorated Carbon Membranes for CO₂ Electroreduction to Methanol. *J. Am. Chem. Soc.* **2019**, *141*, 12717–12723. [[CrossRef](#)] [[PubMed](#)]
125. Han, L.; Song, S.; Liu, M.; Yao, S.; Liang, Z.; Cheng, H.; Ren, Z.; Liu, W.; Lin, R.; Qi, G.; et al. Stable and Efficient Single-Atom Zn Catalyst for CO₂ Reduction to CH₄. *J. Am. Chem. Soc.* **2020**, *142*, 12563–12567. [[CrossRef](#)]
126. Wang, Q.; Zhang, Z.; Cai, C.; Wang, M.; Zhao, Z.L.; Li, M.; Huang, X.; Han, S.; Zhou, H.; Feng, Z.; et al. Single Iridium Atom Doped Ni₂P Catalyst for Optimal Oxygen Evolution. *J. Am. Chem. Soc.* **2021**, *143*, 13605–13615. [[CrossRef](#)]
127. Intikhab, S.; Rebollar, L.; Li, Y.; Pai, R.; Kalra, V.; Tang, M.H.; Snyder, J.D. Caffeinated Interfaces Enhance Alkaline Hydrogen Electrocatalysis. *ACS Catal.* **2020**, *10*, 6798–6802. [[CrossRef](#)]
128. Vij, V.; Sultan, S.; Harzandi, A.M.; Meena, A.; Tiwari, J.N.; Lee, W.G.; Yoon, T.; Kim, K.S. Nickel-Based Electrocatalysts for Energy-Related Applications: Oxygen Reduction, Oxygen Evolution, and Hydrogen Evolution Reactions. *ACS Catal.* **2017**, *7*, 7196–7225. [[CrossRef](#)]
129. Nasim, F.; Ali, H.; Nadeem, M.A.; Nadeem, M.A. High-Performance FeOx@CoOx/NC Electrocatalysts for the Oxygen Reduction Reaction in Alkaline Media. *Sustain. Energy Fuels* **2022**, *7*, 190–200. [[CrossRef](#)]
130. Gopi, S.; Panda, A.; Ramu, A.G.; Theerthagiri, J.; Kim, H.; Yun, K. Bifunctional Electrocatalysts for Water Splitting from a Bimetallic (V Doped-NixFey) Metal–Organic Framework MOF@Graphene Oxide Composite. *Int. J. Hydrogen Energy* **2022**, *47*, 42122–42135. [[CrossRef](#)]
131. Oh, N.K.; Seo, J.; Lee, S.; Kim, H.J.; Kim, U.; Lee, J.; Han, Y.K.; Park, H. Highly Efficient and Robust Noble-Metal Free Bifunctional Water Electrolysis Catalyst Achieved via Complementary Charge Transfer. *Nat. Commun.* **2021**, *12*, 4606. [[CrossRef](#)]
132. You, B.; Sun, Y. Innovative Strategies for Electrocatalytic Water Splitting. *Acc. Chem. Res.* **2018**, *51*, 1571–1580. [[CrossRef](#)]
133. Yan, Y.; Xia, B.Y.; Zhao, B.; Wang, X. A Review on Noble-Metal-Free Bifunctional Heterogeneous Catalysts for Overall Electrochemical Water Splitting. *J. Mater. Chem. A* **2016**, *4*, 17587–17603. [[CrossRef](#)]
134. Yu, X.; Zhao, J.; Zheng, L.R.; Tong, Y.; Zhang, M.; Xu, G.; Li, C.; Ma, J.; Shi, G. Hydrogen Evolution Reaction in Alkaline Media: Alpha- or Beta-Nickel Hydroxide on the Surface of Platinum? *ACS Energy Lett.* **2018**, *3*, 237–244. [[CrossRef](#)]
135. Asnavandi, M.; Yin, Y.; Li, Y.; Sun, C.; Zhao, C. Promoting Oxygen Evolution Reactions through Introduction of Oxygen Vacancies to Benchmark NiFe-OOH Catalysts. *ACS Energy Lett.* **2018**, *3*, 1515–1520. [[CrossRef](#)]
136. Zhou, K.L.; Wang, Z.; Han, C.B.; Ke, X.; Wang, C.; Jin, Y.; Zhang, Q.; Liu, J.; Wang, H.; Yan, H. Platinum Single-Atom Catalyst Coupled with Transition Metal/Metal Oxide Heterostructure for Accelerating Alkaline Hydrogen Evolution Reaction. *Nat. Commun.* **2021**, *12*, 3783. [[CrossRef](#)]
137. Zhang, J.; Lian, J.; Jiang, Q.; Wang, G. Boosting the OER/ORR/HER Activity of Ru-Doped Ni/Co Oxides Heterostructure. *Chem. Eng. J.* **2022**, *439*, 135634. [[CrossRef](#)]
138. Liu, M.; Min, K.A.; Han, B.; Lee, L.Y.S. Interfacing or Doping? Role of Ce in Highly Promoted Water Oxidation of NiFe-Layered Double Hydroxide. *Adv. Energy Mater.* **2021**, *11*, 202101281. [[CrossRef](#)]
139. Zeng, K.; Tian, M.; Chen, X.; Zhang, J.; Rummeli, M.H.; Strasser, P.; Sun, J.; Yang, R. Strong Electronic Coupling between Single Ru Atoms and Cobalt-Vanadium Layered Double Hydroxide Harness Efficient Water Splitting. *Chem. Eng. J.* **2023**, *452*, 139151. [[CrossRef](#)]
140. Jun, S.E.; Choi, S.; Choi, S.; Lee, T.H.; Kim, C.; Yang, J.W.; Choe, W.O.; Im, I.H.; Kim, C.J.; Jang, H.W. Direct Synthesis of Molybdenum Phosphide Nanorods on Silicon Using Graphene at the Heterointerface for Efficient Photoelectrochemical Water Reduction. *Nano-Micro Lett.* **2021**, *13*, 81. [[CrossRef](#)]
141. Xin, Y.; Kan, X.; Gan, L.Y.; Zhang, Z. Heterogeneous Bimetallic Phosphide/Sulfide Nanocomposite for Efficient Solar-Energy-Driven Overall Water Splitting. *ACS Nano* **2017**, *11*, 10303–10312. [[CrossRef](#)] [[PubMed](#)]
142. Kwon, K.C.; Kim, C.; Van Le, Q.; Gim, S.; Jeon, J.M.; Ham, J.Y.; Lee, J.L.; Jang, H.W.; Kim, S.Y. Synthesis of Atomically Thin Transition Metal Disulfides for Charge Transport Layers in Optoelectronic Devices. *ACS Nano* **2015**, *9*, 4146–4155. [[CrossRef](#)] [[PubMed](#)]
143. Zhou, D.; Wang, Z.; Long, X.; An, Y.; Lin, H.; Xing, Z.; Ma, M.; Yang, S. One-Pot Synthesis of Manganese Oxides and Cobalt Phosphides Nanohybrids with Abundant Heterointerfaces in an Amorphous Matrix for Efficient Hydrogen Evolution in Alkaline Solution. *J. Mater. Chem. A* **2019**, *7*, 22530–22538. [[CrossRef](#)]
144. Wang, K.; Wang, X.; Li, Z.; Yang, B.; Ling, M.; Gao, X.; Lu, J.; Shi, Q.; Lei, L.; Wu, G.; et al. Designing 3d Dual Transition Metal Electrocatalysts for Oxygen Evolution Reaction in Alkaline Electrolyte: Beyond Oxides. *Nano Energy* **2020**, *77*, 105162. [[CrossRef](#)]
145. Peng, L.; Shah, S.S.A.; Wei, Z. Recent Developments in Metal Phosphide and Sulfide Electrocatalysts for Oxygen Evolution Reaction. *Cuihua Xuebao/Chin. J. Catal.* **2018**, *39*, 1575–1593. [[CrossRef](#)]
146. Wang, T.; Cao, X.; Jiao, L. Ni₂P/NiMoP Heterostructure as a Bifunctional Electrocatalyst for Energy-Saving Hydrogen Production. *eScience* **2021**, *1*, 69–74. [[CrossRef](#)]
147. Ji, X.; Lin, Y.; Zeng, J.; Ren, Z.; Lin, Z.; Mu, Y.; Qiu, Y.; Yu, J. Graphene/MoS₂/FeCoNi(OH)_x and Graphene/MoS₂/FeCoNiP_x Multilayer-Stacked Vertical Nanosheets on Carbon Fibers for Highly Efficient Overall Water Splitting. *Nat. Commun.* **2021**, *12*, 1380. [[CrossRef](#)]
148. Song, Y.; Cheng, J.; Liu, J.; Ye, Q.; Gao, X.; Lu, J.; Cheng, Y. Modulating Electronic Structure of Cobalt Phosphide Porous Nanofiber by Ruthenium and Nickel Dual Doping for Highly-Efficiency Overall Water Splitting at High Current Density. *Appl. Catal. B Environ.* **2021**, *298*, 120488. [[CrossRef](#)]

149. Wang, D.; Luo, D.; Zhang, Y.; Zhao, Y.; Zhou, G.; Shui, L.; Chen, Z.; Wang, X. Deciphering Interpenetrated Interface of Transition Metal Oxides/Phosphates from Atomic Level for Reliable Li/S Electrocatalytic Behavior. *Nano Energy* **2021**, *81*, 105602. [[CrossRef](#)]
150. Zhang, Y.; Gao, L.; Hensen, E.J.M.; Hofmann, J.P. Evaluating the Stability of Co₂P Electrocatalysts in the Hydrogen Evolution Reaction for Both Acidic and Alkaline Electrolytes. *ACS Energy Lett.* **2018**, *3*, 1360–1365. [[CrossRef](#)]
151. Yu, X.; Zhao, J.; Johnsson, M. Interfacial Engineering of Nickel Hydroxide on Cobalt Phosphide for Alkaline Water Electrocatalysis. *Adv. Funct. Mater.* **2021**, *31*, 2101578. [[CrossRef](#)]
152. Jin, S. Are Metal Chalcogenides, Nitrides, and Phosphides Oxygen Evolution Catalysts or Bifunctional Catalysts? *ACS Energy Lett.* **2017**, *2*, 1937–1938. [[CrossRef](#)]
153. Chen, Z.; Duan, X.; Wei, W.; Wang, S.; Ni, B.J. Recent Advances in Transition Metal-Based Electrocatalysts for Alkaline Hydrogen Evolution. *J. Mater. Chem. A* **2019**, *7*, 14971–15005. [[CrossRef](#)]
154. Hu, Z.; Liu, Q.; Chou, S.L.; Dou, S.X. Advances and Challenges in Metal Sulfides/Selenides for Next-Generation Rechargeable Sodium-Ion Batteries. *Adv. Mater.* **2017**, *29*, 1700606. [[CrossRef](#)]
155. Liu, W.; Wang, X.; Wang, F.; Liu, X.; Zhang, Y.; Li, W.; Guo, Y.; Yin, H.; Wang, D. Electrochemical Hydroxidation of Sulfide for Preparing Sulfur-Doped NiFe (Oxy) Hydroxide towards Efficient Oxygen Evolution Reaction. *Chem. Eng. J.* **2023**, *454*, 140030. [[CrossRef](#)]
156. Zhang, L.; Zheng, Y.; Wang, J.; Geng, Y.; Zhang, B.; He, J.; Xue, J.; Frauenheim, T.; Li, M. Ni/Mo Bimetallic-Oxide-Derived Heterointerface-Rich Sulfide Nanosheets with Co-Doping for Efficient Alkaline Hydrogen Evolution by Boosting Volmer Reaction. *Small* **2021**, *17*, 2006730. [[CrossRef](#)]
157. Yao, N.; Li, P.; Zhou, Z.; Zhao, Y.; Cheng, G.; Chen, S.; Luo, W. Synergistically Tuning Water and Hydrogen Binding Abilities Over Co₄N by Cr Doping for Exceptional Alkaline Hydrogen Evolution Electrocatalysis. *Adv. Energy Mater.* **2019**, *9*, 1902449. [[CrossRef](#)]
158. Diao, J.; Qiu, Y.; Liu, S.; Wang, W.; Chen, K.; Li, H.; Yuan, W.; Qu, Y.; Guo, X. Interfacial Engineering of W₂N/WC Heterostructures Derived from Solid-State Synthesis: A Highly Efficient Trifunctional Electrocatalyst for ORR, OER, and HER. *Adv. Mater.* **2020**, *32*, 1905679. [[CrossRef](#)]

Disclaimer/Publisher's Note: The statements, opinions and data contained in all publications are solely those of the individual author(s) and contributor(s) and not of MDPI and/or the editor(s). MDPI and/or the editor(s) disclaim responsibility for any injury to people or property resulting from any ideas, methods, instructions or products referred to in the content.